JAERI-M
93-037

PROGRESS REPORT ON SAFETY RESEARCH ON HIGH-LEVEL WASTE MANAGEMENT FOR THE PERIOD APRIL 1991 TO MARCH 1992

March 1993

(Eds.) Susumu MURAOKA, Muneaki SENOO and Yoshii KOBAYASHI

日本原子力研究所
Japan Atomic Energy Research Institute

JAERI-Mレポートは，日本原子力研究所が不定期に公刊している研究報告書です。
入手の問合わせは，日本原子力研究所技術情報部情報資料課（〒319-11茨城県那珂郡東海村）あて，お申しこしください。なお，このほかに財団法人原子力弘済会資料センター（〒319-11 茨城県那珂郡東海村日本原子力研究所内）で複写による実費頒布をおこなっております。

JAERI-M reports are issued irregularly.
Inquiries about availability of the reports should be addressed to Information Division Department of Technical Information, Japan Atomic Energy Research Institute, Tokai-mura, Naka-gun, Ibaraki-ken 319-11, Japan.

編集兼発行　日本原子力研究所
印　　刷　いばらき印刷㈱

JAERI-M 93-037

Progress Report on Safety Research on High-Level Waste Management for the Period April 1991 to March 1992

(Eds.) Susumu MURAOKA, Muneaki SENOO and Yoshii KOBAYASHI

Department of Environmental Safety Research
Tokai Research Establishment
Japan Atomic Energy Research Institute
Tokai-mura, Naka-gun, Ibaraki-ken

(Received January 29, 1993)

Research on high-level waste management at the Engineered Barrier Materials Laboratory, Environmental Geochemistry Laboratory and Environmental Radiochemistry Laboratory of the Department of Environmental Safety Research, JAERI in the fiscal year of 1991 are described.

The topics are as follows:

1) As for waste forms and engineered barrier material, performance assessment studies on glass, ceramic and buffer materials were carried out.
2) In the safety evaluation study for geological disposal, behavior of radionuclide in deep underground water, nuclide migration in-situ and natural groundwater flow system were studied.
3) Changes in layer charge of smectite, alteration of uranium mineral and uranium fixation in uranium ore were examined as a natural analogue study.

Keywords: High-Level Waste, Waste Forms, Engineered Barrier Material, Glass, Ceramic, Migration, Retardation, Groundwater, Uranium, Natural Analogue

JAERI-M 93-037

高レベル廃棄物処理処分の安全性に関する平成3年度報告書

日本原子力研究所東海研究所環境安全研究部
（編）村岡　進・妹尾　宗明・小林　義威

（1993年1月29日受理）

人工バリア研究室，深地処分研究室及び環境放射化学研究室において，平成3年度に実施した高レベル廃棄物処理処分の安全性に関する研究成果をまとめた。

その内容は次の通りである。

1）廃棄物固化体及び人工バリア材の研究開発では，ガラス固化体，セラミック固化体及び緩衝材の性能評価試験を継続した。

2）地層処分の安全評価試験では，地下水中での放射性核種の挙動，原位置条件下における核種の移行試験を実施した。また，天然地下水の流動に関する研究を進めた。

3）ナチュラルアナログ研究として，続成変質中のスメクタイトの性質，ウラン鉱床中のウラン鉱物の変質，固定化に関する研究を実施した。

東海研究所：〒319－11　茨城県那珂郡東海村白方字白根2－4

Contents

Introduction
1. Research and Development of Waste Forms and Engineered Barrier Materials 1
1.1 Performance of Glass Waste Forms 1
1.1.1 Effects of Alpha Decay on the Properties of Actual Nuclear Waste Glass 1
1.1.2 Effects of Alpha-Decay on Microstructure of Simulated High-Level Waste Glass 3
1.1.3 Time-dependence of Volatilization of ^{137}Cs and ^{106}Ru over High-Level Waste Glass in a Canister 6
1.2 Performances of Ceramic Waste Forms 12
1.2.1 Long-term Integrity of Curium-doped Synroc Containing Sodium-free PW-4b Waste 12
1.2.2 Durability of An $La_2Zr_2O_7$ Waste Form in Water 18
1.3 Performance of Engineered Barrier Materials 24
1.3.1 Sorption Characteristics of Neptunium by Smectite 24
2. Safety Evaluation Study for Geological Disposal 28
2.1 Behavior of Radionuclides in Underground Water 28
2.1.1 Effects of Temperature and pH on Crystallization Kinetics of Goethite from Ferrihydrite 28
2.1.2 Diffusion of Strontium in Rock Matrix 31
2.2 Radionuclide Migration Tests under In-situ Conditions 36
2.2.1 Migration Experiments under Deep Geological Conditions ... 36
2.2.2 Glass Block Site Experiment 42
2.3 Study on Natural Groundwater Flow System 49
3. Natural Analogue Study 50
3.1 Changes in Layer Charge of Smectites and Smectite Layers of Illite/Smectite in Diagenetic Alteration 50
3.2 Alteration of Uranium Minerals in the Unweathered Zone 55
3.3 Uranium Fixation During Chlorite Weathering at Koongarra, Australia 60

目　　次

まえがき
1. 廃棄物固化体と人工バリア材料に関する研究開発 …… 1
1.1 ガラス固化体の性能 …… 1
1.1.1 実廃棄物ガラス固化体性質に及ぼすアルファ崩壊の影響 …… 1
1.1.2 模擬高レベル廃棄物ガラスの微細構造に及ぼすアルファ崩壊の影響 …… 3
1.1.3 高レベル廃棄物ガラスからの^{137}Cs及び^{106}Ruの蒸発の時間依存性 …… 6
1.2 セラミック固化体の開発 …… 12
1.2.1 PW－4b廃棄物を含有するキュリウム添加シンロックの長期安定性 …… 12
1.2.2 $La_2Zr_2O_7$廃棄物固化体の耐久性 …… 18
1.3 人工バリア材の性能 …… 24
1.3.1 スメクタイトによるネプツニウムの吸着 …… 24
2. 地層処分の安全性評価研究 …… 28
2.1 深層地下水中における放射性核種の挙動 …… 28
2.1.1 非晶質水酸化鉄から針鉄鉱への結晶化機構に及ぼす温度とpHの影響 …… 28
2.1.2 岩石マトリックス中でのストロンチウムの拡散 …… 31
2.2 原位置条件下における核種移行試験 …… 36
2.2.1 カナダチョークリバー研究所におけるガラスブロック浸出核種の移行挙動 …… 36
2.2.2 ＵＲＬ（カナダ）における深地下条件核種移行試験 …… 42
2.3 天然地下水の流動に関する研究 …… 49
3. ナチュラルアナログ研究 …… 50
3.1 続成変質中のスメクタイト及びイライト／スメクタイトのスメクタイトの層間電荷の変化 …… 50
3.2 未風化域におけるウラン鉱物の変質 …… 55
3.3 オーストラリアクーンガラウラン鉱床におけるクロライトの変質過程でのウランの固定化 …… 60

Introduction

In order to achieve the safe disposal of high-level radioactive waste, it is necessary to promote the development of waste management and safety assessment methodology.

The Japan Atomic Energy Research Institute (JAERI) has conducted safety assessment study and development of new technology to contribute the establishment of national system for the high-level radioactive waste management in Japan.

This report summarizes the status and results of studies performed in the fiscal year 1991 at the Engineered Barrier Materials Laboratory, Environmental Geochemistry Laboratory and Environmental Radiochemistry Laboratory of the Department of Environmental Safety Research, JAERI.

The progress report series have been issued in the following numbers; JAERI-M 82-145, 83-076, 84-133, 85-090, 86-131, 87-131, 88-201, 89-192, 91-019 and 92-022.

1. Research and Development of Waste Forms and Engineered Barrier Materials

1.1 Performance of Glass Waste Forms

1.1.1 Effects of Alpha Decay on the Properties of Actual Nuclear Waste Glass

T. Banba and S. Matsumoto

A variety of different types of radiation can affect chemical and physical properties of glasses. Nuclear waste glasses represent a system in which many different types of radiation can coexist. The radiation effects involved result from he emission of alpha and beta particles, and from gamma rays and neutrons from the decaying radionuclides. Most of the effects involving atomic displacements are induced by passage of these particles through the glass[1]. From displacement rate calculations[2], the most severe damage results from the alpha particle and recoil nucleus from alpha decay of actinides. Generally, the effects of alpha decay are simulated by actinide-doping techniques.

In the present study, an accelerated experiment using the actinide doping technique was performed to investigate the effects of alpha decay on the performance and properties of actual nuclear waste glass at high radiaion doses. A fully active borosilicate waste glass, containing the actual high-level radioactive liquid waste (HLLW) generated from the Tokai Reprocessing Plant of PNC (Power Reactor and Nuclear Fuel Development Corporation), was prepared by the vitrification apparatus[3] of JAERI (Japan Atomic Energy Research Institute), and a powder mixture of the grinding fully active glass and curium oxide ($^{244}CmO_2$) was melted in the platinum crucibles of 14 mm in diameter at 1200°C for 2 hrs. The glass in the crucible was held at 600°C for 1 hr, and then slowly cooled to room temperature. The radioactivity concentration of ^{244}Cm was 1.0×10^{10} Bq/g-glass at the date of preparation. The glass was cut into disks of 5 mm in thickness, and the homogeneity of glass samples were confirmed by the density measurement, heat load measurement and alpha autoradiography. Each sample was stored in a helium leak-protective capsule until the tests.

Several glass samples were used for the characterization tests at a

cumulative alpha decay dose corresponding to each equivalent age. The properties of the irradiated samples were investigated by the mass spectrometer for helium determination, the optical microscope, the electron probe microanalyzer (EPMA), the densitometer, the Soxhlet and MCC-1 type leaching test apparatus.

It was found by measuring the amount of helium released from the glass samples that over 99% of helium remained in the matrix at room temperature. The total amount of helium generated in the sample was obtained from the amount of helium released from the sample held at 800°C for 15 min and that at room temperature. The density of the sample decreased slightly with the increase of cumulative alpha decays and the decrement of 0.45% was observed at a dose of 6.5×10^{17} alpha-decays/g, corresponding to an equivalent age of about 10^4 yrs. The increase in leach rates, based on the weight losses in the Soxhlet type test (100°C, 7 days), was not more than 30% up to a dose of 6.5×10^{17} alpha-decays/g (equivalent age, about 10^4 yrs). Optical and scanning electron micrographs showed that no cracks were observed on all samples having up to a dose of 6.5×10^{17} alpha-decays/g.

References

1. W.J. Weber, F.P. Roberts, Nucl. Technol., 60, 178 (1983).
2. I. Manning, G.P. Mueller, Comp. Phys. Comn., 7, 85 (1974).
3. S. Tashiro et al., JAERI-M 84-044 (1984).

1.1.2 Effects of Alpha-Decay on Microstructure of Simulated High-Level Waste Glass

Y. Inagaki, H. Furuya and T. Banba

The radiation effects on the properties of high-level waste glasses have been investigated using some irradiation techniques. Experimental data of radiation-induced changes in volume, stored energy, and mechanical properties have been obtained by a number of investigators, but the mechanism of these changes has not been well understood. It has been generally assumed that most radiation-induced changes in the waste glass properties are related to damages from direct atomic displacements produced by elastic collisions and from electronic excitations resulting from ionization processes. In the waste glass, helium atoms are generated from alpha-decay of actinides and it is expected that helium bubbles are formed after exceeding its amount beyond the solubility limit in the waste glass[1]. Helium bubble formation has a great influence especially on volume and mechanical properties of the waste glass[2,3].

The purpose of this study is to investigate the microstructural changes of the irradiated waste glass. The microstructural changes of a simulated waste glass doped with ^{238}Pu and ^{244}Cm were observed by use of a preshadowed carbon replica technique in combination with scanning electron microscopy (SEM). The irradiated glass was annealed and its microstructural changes after annealing were observed by use of the same technique. On the basis of the results, the behavior of helium bubbles was discussed.

Figure 1 shows microstructure of the glass irradiated at a dose of 2.75×10^{25} alpha-decays/m^3. In the irradiated glass, some bubbles were observed. The average bubble radius and the bubble density were 0.46 μm and 1×10^{17} bubbles/m^3, respectively. Using these observed values, the volume change of the glass resulting from the bubble formation was estimated to be +0.5%. This value of +0.5% was close to the volume change of the irradiated glass measured in our previous study[4], which suggests a large portion of the volume change results from bubble formation.

The average bubble radius during annealing at 673 K as a function of annealing time is shown in Fig. 2 as open circles, in which the error bar represents the mean error. The bubble radius was observed to decrease with annealing time. The bubble behavior during annealing was analyzed on the basis of the helium diffusion model with two chemical processes,

i.e. trapping at bubbles and resolution from bubbles into glass matrix[5,6]. The diffusion equation is described by,

$$\frac{\partial C}{\partial t} = D\left(\frac{\partial^2 C}{\partial r^2} + \frac{1}{r}\frac{\partial C}{\partial r} + \frac{\partial^2 C}{\partial z^2}\right) - gC + bM, \qquad (1)$$

where C is the concentration of helium in glass matrix, M is the number of helium atoms trapped in bubbles per unit glass volume, t is the annealing time, r is radial position in a specimen, z is vertical position in a specimen, D is the diffusion coefficient of helium in glass matrix, g is the trapping rate constant and b is the re-solution rate constant. The balance for the trapped helium is described by,

$$\frac{\partial M}{\partial t} = gC - bM. \qquad (2)$$

Values of D, g and b, which had been obtained experimentally in our previous study on the helium release[7], were applied to the calculation.

The bubble radius at 673 K as a function of annealing time was calculated using the above model. The calculated curve is shown in Fig. 2 as a solid line. The agreement between the calculated and observed bubble radius was relatively good.

References

1. S. Sato et al., J. Nucl. Mater., 152, 489 (1988).
2. W.J. Weber, Nucl. Instr. and Meth., B32, 471 (1988).
3. W.J. Weber, Hj. Matzke, PNL-SA-13907 (1986).
4. Y. Inagaki, T. Banba et al., JAERI-M 90-225 (1990).
5. D.R. Olander, Fundamental Aspects of Nuclear Reactor Fuel Elements, ERDA, Springfield Virginia, p.307 (1976).
6. R.P. Turcotte, BNWL-2051 (1976).
7. K. Morikawa et al., J. Nucl. Sci. Technol., to be published.

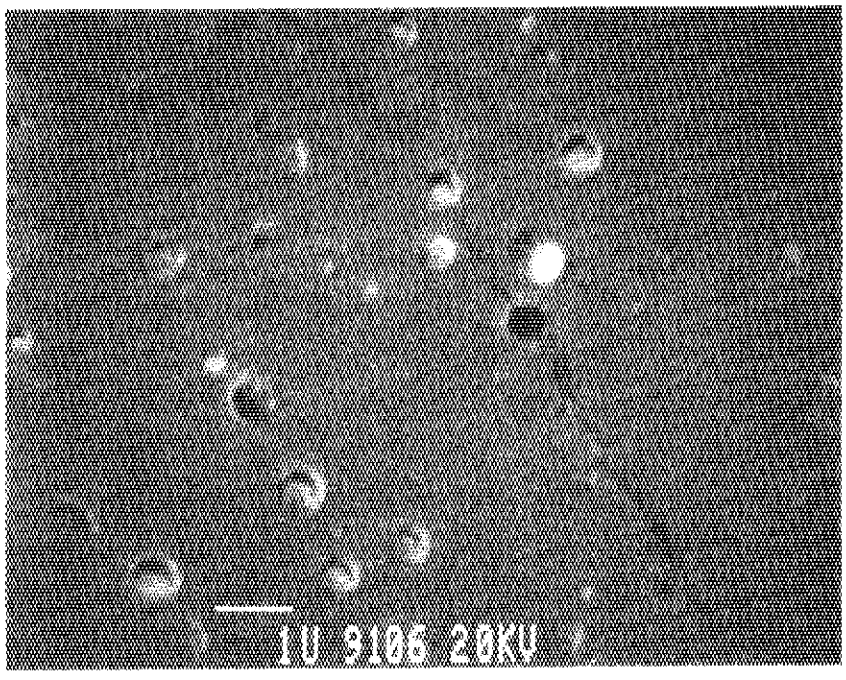

Fig. 1 A SEM micrograph of fractured surface for the simulated waste glass irradiated at a dose of 2.75×10^{25} alpha-decays/m^3. White scale bar = 1 μm.

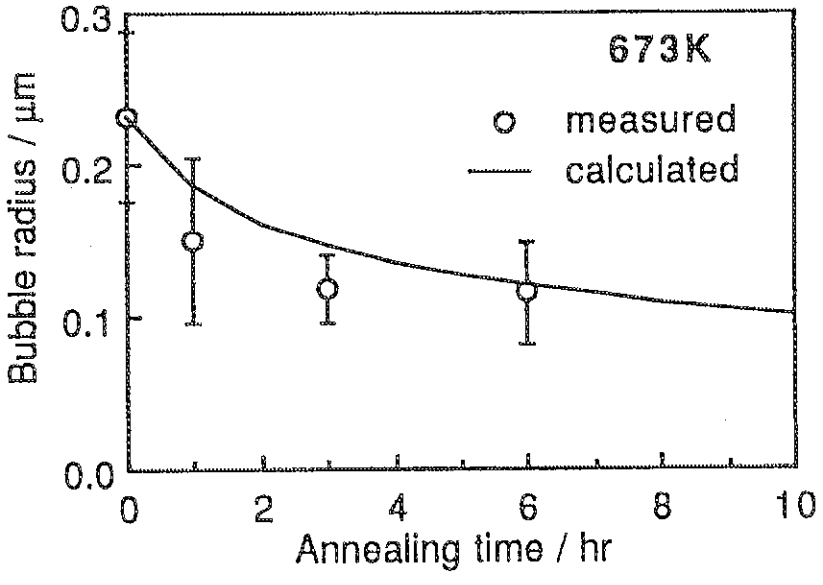

Fig. 2 The average bubble radius during annealing at 673K as a function of annealing time.

1.1.3 Time-dependence of Volatilization of ^{137}Cs and ^{106}Ru over High-Level Waste Glass in a Canister

H. Kamizono

Introduction

In our previous studies[1-4], the time- and temperature-dependence of the volatility of ^{137}Cs, ^{134}Cs and ^{106}Ru in an almost closed stainless steel canister was experimentally observed. This was useful for predicting air contamination in the plenum of the canister placed in an operational storage facility. The purpose of the present study[5] is to describe a mathematical formula which expresses the time-dependence of the volatility of the radionuclides. The formula is also used for predicting the effects of the surface area of the glass and the plenum volume of the canister on the concentration excursion of the radionuclides. This is, in other words, a possible way to predict the effects of different plenum sizes on the rate of the air contamination in the canister.

Analysis

We assume that the detailed mechanisms involved in the present study are as illustrated in Ref. 3. The forward step contains two paths in series. One is the diffusion of the radionuclides from inside the glass to its surface, and the other is the reaction of the radionuclides on the glass surface with other elements. It has been reported that Cs volatilizes in borate form (e.g., $CsBO_2$), and Ru, in oxide form (mainly as RuO_4). Therefore, the reaction between Cs and B and the oxidation of Ru or RuO_2 into RuO_4 may occur on the glass surface.

The formation of a surface layer on the glass is taken into account in this paper, since the convection of the glass is very slow at 600°C and a non-volatile surface layer is likely to remain on the surface for a relatively long time.

On the other hand, the backward step may consist of three paths in parallel. The first is the precipitation of vapor directly onto the glass surface. The second is the reaction of vapor with the stainless steel canister. The third is the precipitation which causes solid materials to

form in the air, coarsen, and then fall onto the glass surface.

The mechanisms described above are complicated, but the overall change of the air contamination in the canister can be basically described by a mathematical formula,

$$VdC/dt = S_1k_1(k_2t + k_3)^{-1/2} - S_1C(k_4 + S_2k_5/S_1 + Vk_6/S_1) \quad (1)$$

where V (1007 cm^3) is the plenum volume, C (Bq/cm^3) is the normalized concentration of a volatilized element in the plenum, S_1 (51.5 cm^2) is the surface area of the glass exposed to the air, S_2 (554 cm^2) is the inner surface area of the canister, k_1 ($Bq\ cm^{-2}hour^{-1}$) is the forward rate of volatilization, k_2 ($hour^{-1}$) and k_3 (unitless) are arbitrary constants, k_4 and k_5 (both in units of cm $hour^{-1}$) are the backward rates of precipitation onto the glass surface and onto the inner surface of the canister, respectively. The constant k_6 ($hour^{-1}$) is the rate of coarsening in the plenum and t is time once the glass reaches 600°C. The combination of the constants of $k_4 + S_2k_5/S_1 + Vk_6/S_1$ is later replaced with X in the numerical analysis. We assume that a surface layer forms on the glass and serves as a barrier against diffusion of the radionuclides, and therefore the forward rate of volatilization can be expressed by the term of $k_1(k_2t + k_3)^{-1/2}$ in Eq.1. Note that k_3 is equal to or greater than unity, which represents the thickness of the surface layer formed before t = 0. When t = 0, C = 0 and k_3 = 1, Eq.1 gives the initial tangent of a fitting curve. Equation 1 is numerically integrated by the Runge-Kutta method with arbitrary constants.

Results

Determination of the constants

The constants in Eq.1 were determined by the best fits of Eq.1 to the data in Ref. 3. As for ^{137}Cs, $k_1 = 5.0 \times 10^{-5}$, k_2 = 1, K_3 = 10 and X = 10. As for ^{106}Ru, $K_1 = 3.5 \times 10^{-7}$, $k_2 = k_3$ = 1, and X = 0.25. The forward rate of volatilization k_1 for ^{137}Cs is about 140 times higher than that of ^{106}Ru at 600°C. This is probably because cesium easily diffuses in the glass in comparison with ruthenium. On the other hand, the overall backward precipitation rate X for ^{137}Cs is about 40 times lower than that for ^{106}Ru, meaning that ^{106}Ru is hardly immobilized through the backward

steps at 600°C.

Based on the best fits described above, a standard set of the constants for the following example calculations were determined as $k_1 = 5 \times 10^{-5}$, $k_2 = 1$, $S_1 = 51.5$, $V = 1007$, $C_0 = 0$, $k_3 = 1$, and $X = 1$.

Effects of time on the concentration C

A typical example of the effects of time on the concentration C is observed in Fig. 1. Excursion of C generally shows a maximum value and then a gradual decrease. It will asymptotically converge to zero, not to a positive steady-state concentration.

Effects of k_1 and X on the concentration C

Figure 1 also shows that when the constant K_1 becomes one-tenth of a previous value, it effects a decrease of the maximum C value to one-tenth than before. Figure 2 shows that the constant X is effective to change the maximum C value and also the time in which the maximum C value appears.

Effects of the glass surface area S_1 and the plenum volume V

The role of the two parameters S_1 and V is clear in Eq.1. The increase of S_1 results in an increase of dC/dt, and the increase of V results in a decrease of dC/dt. Figure 3 shows the curves with different V values. Note that when S_1 becomes double, it is comparable to the effect when V is reduced by half.

When the plenum volume of a canister containing HLW glass is assumed to be 3×10^5 cm^3, the ratio of glass-surface-area to plenum-volume is about 0.05 cm^{-1}. This ratio was kept constant in the experiments in Ref. 3.

Discussion and Conclusions

Equation 1 contains an assumption that a surface layer tends to form during heating. Therefore, it is desirable to confirm the presence of the surface layer experimentally. The observation of a diffusion profile on the surface of an HLW glass is one of our future topics.

In this paper, the presence of the surface layer is assumed at a moderate temperature of 600°C. However, when the temperature reaches 1000°C, the convection of the bulk glass occurs considerably and it will

facilitate the mass transport of ^{137}Cs and ^{106}Ru from the inside of the glass to the surface. In this case, the decrease of the concentration C after its maximum value may not be observed.

Finally, it should be noted that when the constants related to the backward step in Eq.1 are time-dependent, then it is also possible to obtain concentration excursion curves which are similar to those in Figs. 2 to 6. Therefore, we have to identify the mechanisms in detail in the future.

References

1. H. Kamizono, S. Kikkawa, S. Tashiro and H. Nakamura, Nucl. Technol., 72(1), 84-88 (1986).
2. H. Kamizono, S. Kikkawa, S. Tashiro, H. Nakamura and H. Kanazawa, J. Nucl. Mater., 149(1), 113-116 (1987).
3. H. Kamizono, S. Kikkawa, Y. Togashi and S. Tashiro, J. Am. Ceram. Soc., 72(8), 1438-1441 (1989).
4. H. Kamizono, in Proceedings of High-Level Radioactive Waste Management, Vol.2, American Nuclear Society, Inc. and American Society of Civil Engineers, Las Vegas, Nevada, April 8-12 (1990).
5. H. Kamizono and S. Muraoka, in Proceedings of SBNWM, France (1991).

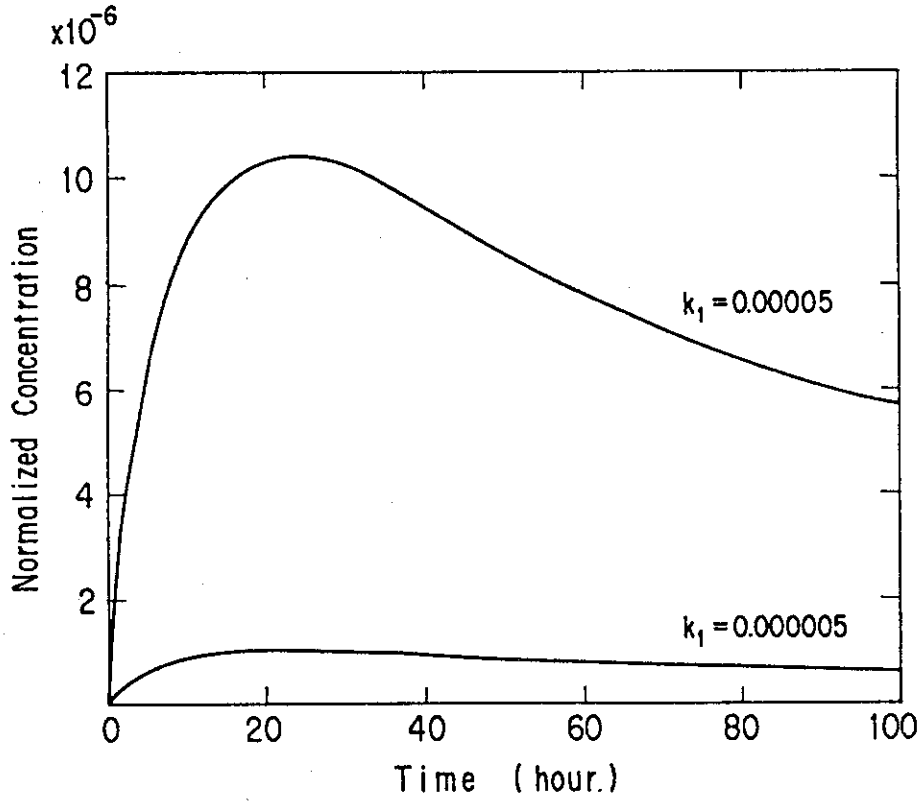

Fig. 1 An example of the calculation with different k_1 values.

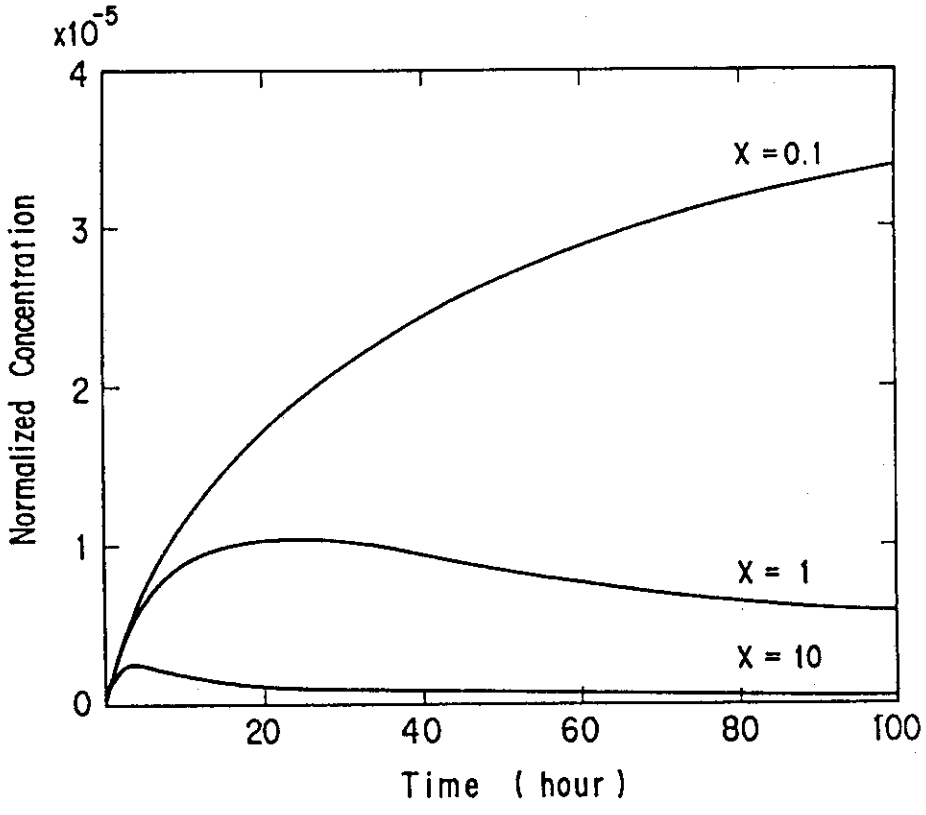

Fig. 2 An example of the calculation with different X values.

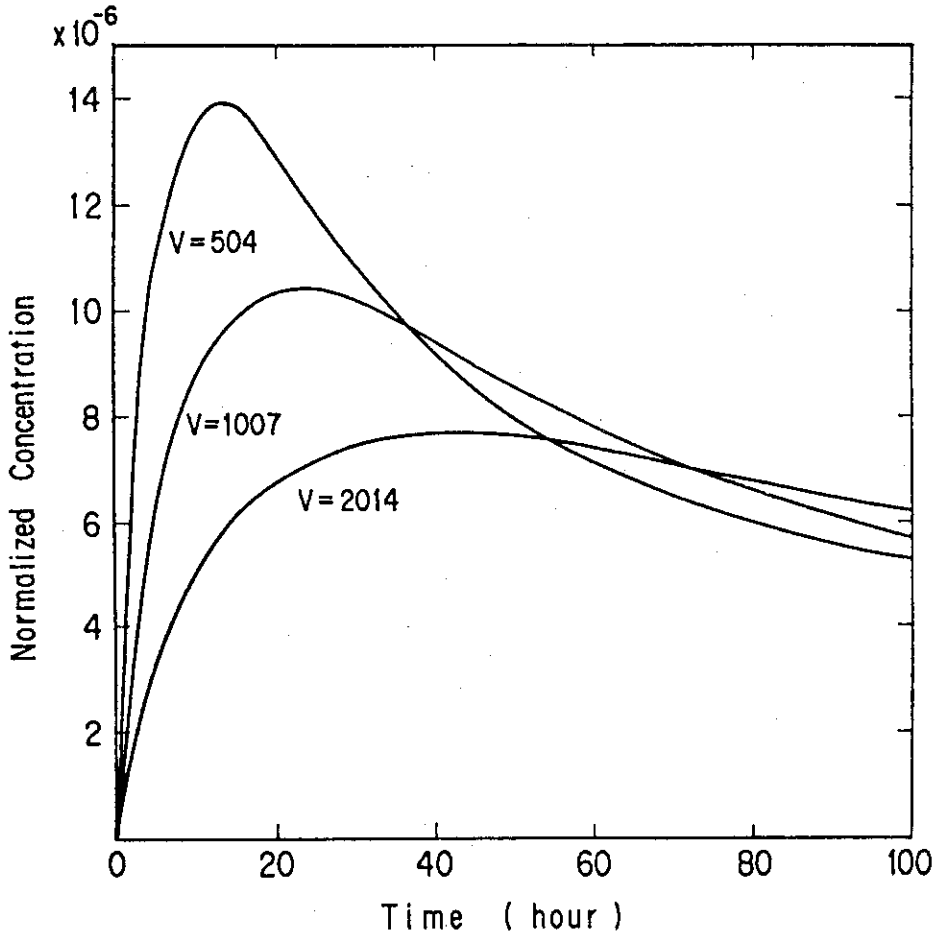

Fig. 3 An example of the calculation with different V values.

1.2 Performance of Ceramic Waste Forms

1.2.1 Long-term Integrity of Curium-doped Synroc Containing Sodium-free PW-4b Waste

H. Mitamura

Introduction

Existing Japanese HLW contains high concentration of the processing contaminants sodium and iron which stabilizes sodium-rich water-soluble phases and intergranular glasses that degrade the mechanical properties of the waste form. The relative concentration of processing contaminants could be reduced with a minor change in the waste stream in a reprocessing plant to yield a reduced sodium PW-4b waste. For Synroc, this would eliminate sodium-rich soluble phases, and consequently improve its long-term integrity. In a previous report[1], densities of the curium-doped sodium-free PW-4b Synroc, which had accumulated a dose up to 12.4×10^{17} alpha decays$\cdot g^{-1}$ (equivalent age, 16,000 yr), were examined. In the present study, curium-doped PW-4b samples, having now sustained more damage, were subjected to density measurement and leach testing to clarify further self-irradiation effects.

Experimental Method

Density Measurement

The densities of 2-cm-dia. × 1-cm-high cylinders (S90002 and S90005) were periodically measured by the water displacement method. The water was kept at 30°C.

Leach Testing

Thin half-disk specimens of a dose of 15.2×10^{17} alpha decays$\cdot g^{-1}$ (equivalent age, 30,000 years) were leach tested in distilled water at 90°C for two months over four 7-day and a 28-day leach periods. After 2 cm^3 of leachate was collected for pH and Eh measurements, 0.1 cm^3 of concentrated nitric acid was added to the remainder to minimize adsorption of ^{244}Cm and precipitation of nonradioactive elements. The total ^{244}Cm

activity leached from curium-doped specimens was measured by gamma-ray spectrometry, and nonradioactive elements were analyzed by atomic absorption spectroscopy (Cs and Sr) and inductively coupled plasma atomic emission spectrometry (Ca, Ba, and Mo).

Result and Discussion

Density

Figure 1 shows the dependence of densities upon cumulative alpha decays per gram up to a dose of 19×10^{17} alpha decays$\cdot g^{-1}$ (equivalent age, 80,000 yr) for the cylinders S90002 and S90005. If the densities are assumed to decrease with alpha-decay dose in an analogous manner to the curium-doped JW-A Synroc for the doses $<8.5 \times 10^{17}$ alpha decays$\cdot g^{-1}$ (equivalent age, 9,000 yr), then least-squares fitting shows the S90002 and S90005 densities were higher by 0.047 and 0.053 g$\cdot cm^{-3}$, respectively. The fitted values give the solid and the dotted lines in this figure. Extrapolation of these fitted curves leads to the initial densities of 4.354 and 4.360 g$\cdot cm^{-3}$ for the samples S90002 and S90005, respectively. In Fig. 1, the PW-4b samples keep a gradual decrease in density with increasing alpha-decay dose, while the sodium-bearing (JW-A) sample increases the rate of density change at a dose of 8.5×10^{17} alpha decays$\cdot g^{-1}$. This suggests that (macro)cracking due to volume swelling did not occur in the PW-4b samples, and provides further evidence that the mechanical properties of curium-doped Synroc were improved by removal of sodium.

Leach Test

Figure 2 summarizes the leach rates of nonradioactive elements from the 30,000-yr PW-4b specimens with time. For comparison, this figure contains data from the 50-yr samples. Accumulation of alpha decays caused an increase in the leach rates of the soluble indicator elements, particularly cesium. In both cases, the leach rates decrease quickly after the initial 7-day leach period and then continue to decrease with time, albeit at a lower rate. Among these elements, molybdenum gives the highest values of the leach rates. Strontium and calcium tend to be lost at similar rates. The leach rate of cesium, however, became much higher than that of barium in 30,000-yr leaching runs, while in 50-yr leaching runs cesium and barium tend to be leached at similar rates. This implies that

cesium-bearing phase(s) other than hollandite affected cesium leaching since these both elements would be incorporated in hollandite phase. Although intergranular phases were not prevalent in PW-4b samples, these phases are likely to incorporate cesium. It is possible that microcracking may occur although density measurement did not show crack formation.

Figure 3 compares the average leach rate of ^{244}Cm from 30,000-yr samples and the analogous leach rate from 50-yr samples. This figure indicates that accumulation of alpha decays up to 15×10^{17} did not affect curium leach rate. Leachate pH and Eh from 30,000-yr samples is similar to that from 50-yr samples. Curium leach rate is dependent on leachate pH and Eh. This is why the curium leach rates from 50- and 30,000-yr samples were similar.

Conclusion

Concluding remarks of the present study are as follows:

(1) Curium-doped Synroc containing PW-4b HLW, which accumulated alpha decays up to a dose of 19×10^{17} alpha decays$\cdot g^{-1}$, showed a gradual decrease in density up to 2.4%. Density measurement did not indicate occurrence of crack formation.

(2) The leach rates of nonradioactive elements from the 30,000-yr specimens became higher than those from 50-yr specimens, particularly cesium. This implies that microcracking may occur.

(3) Curium leach rate was insensitive to accumulation of alpha decay dose.

Further investigation is continued to clarify the effects of radiation damage on long-term stability of sodium-free Synroc.

Reference

(1) H. Mitamura, S. Matsumoto and T. Tsuboi, "Change in Density in Curium-Doped Titanate Ceramic Containing Sodium-Free High-Level Nuclear Waste", in Progress Report on Safety Research on High-Level Waste Management for the Period April 1990 to March 1991, (Eds., S. Muraoka, M. Senoo and Y. Kobayashi), JAERI-M 92-022, Japan Atomic Energy Research Institute, Tokai (1992).

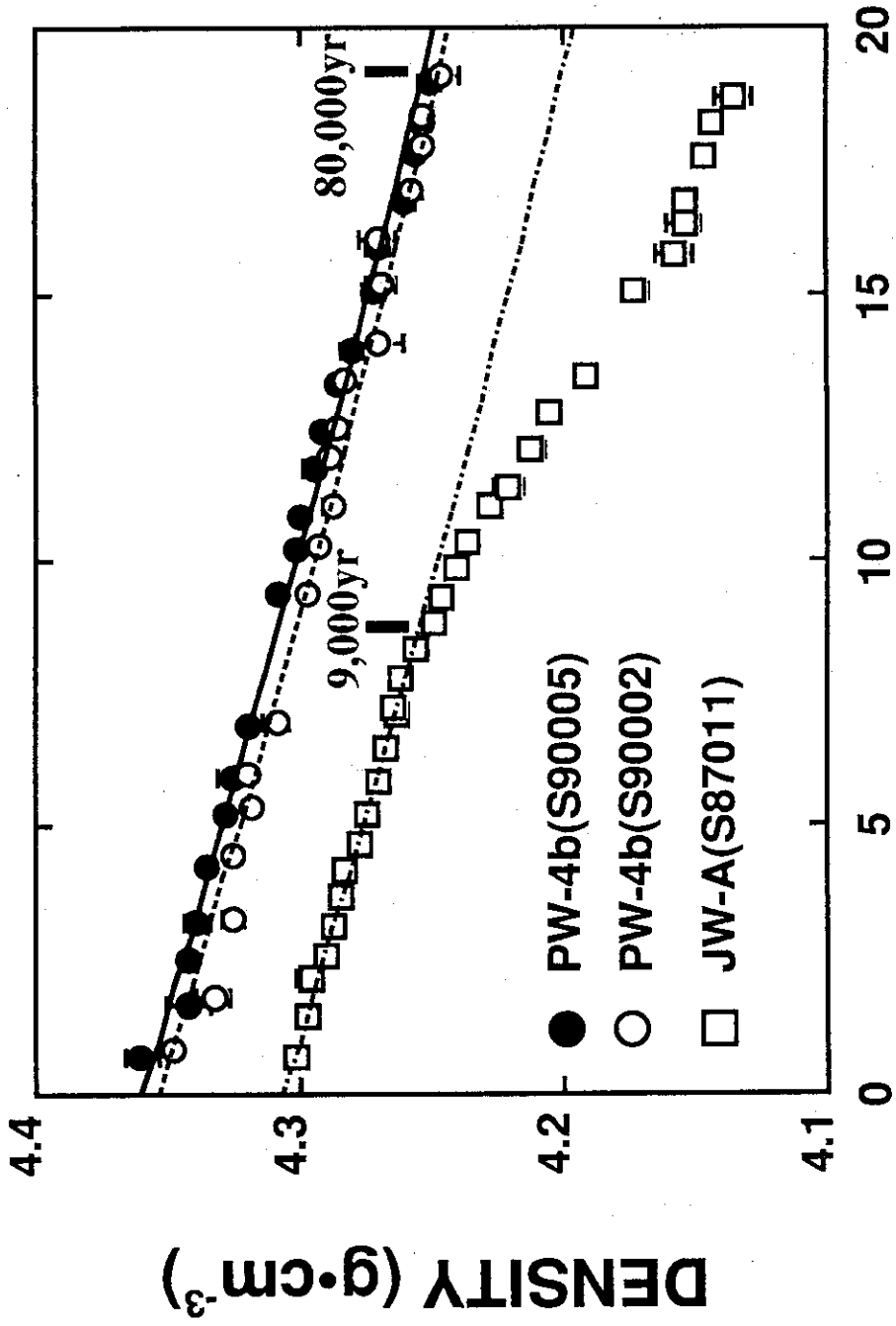

Fig. 1 Densities of two kinds of curium-doped Synroc versus alpha-decay dose. Samples S90002 and S90005 were hot-pressed at 1200°C/29MPa for 1 h and 2 h, respectively.

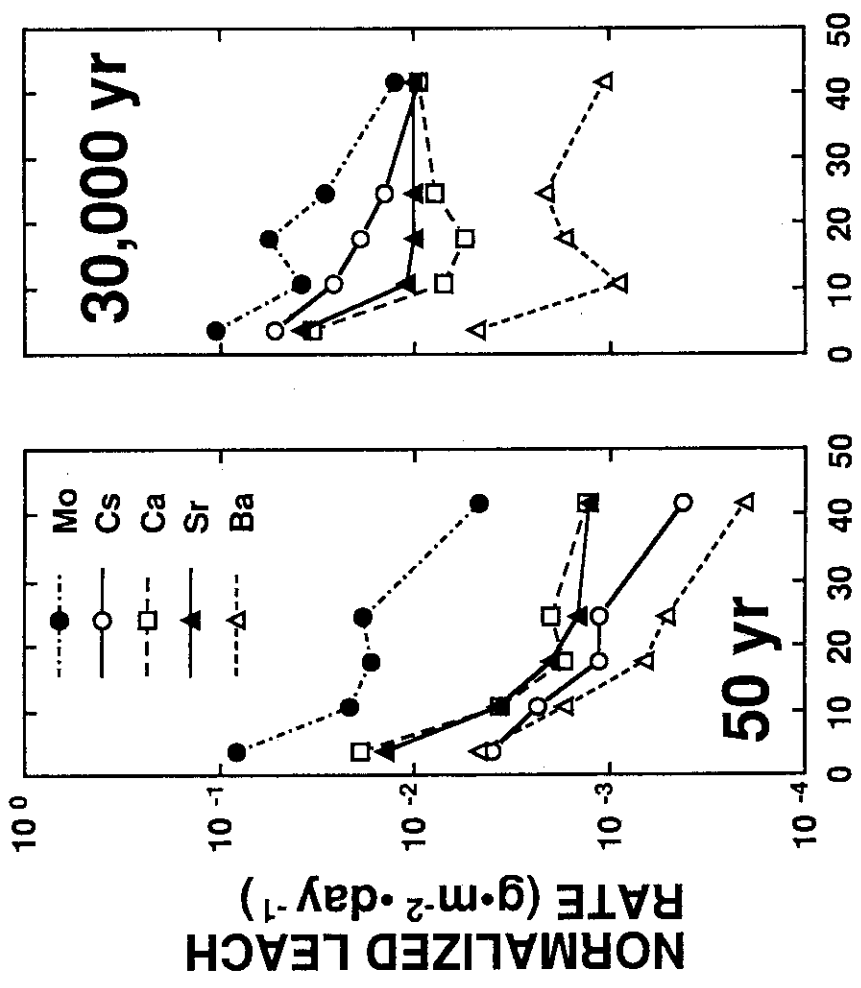

Fig. 2 Comparison of normalized leach rates of nonradioactive elements from 50-yr and 30,000-yr specimens.

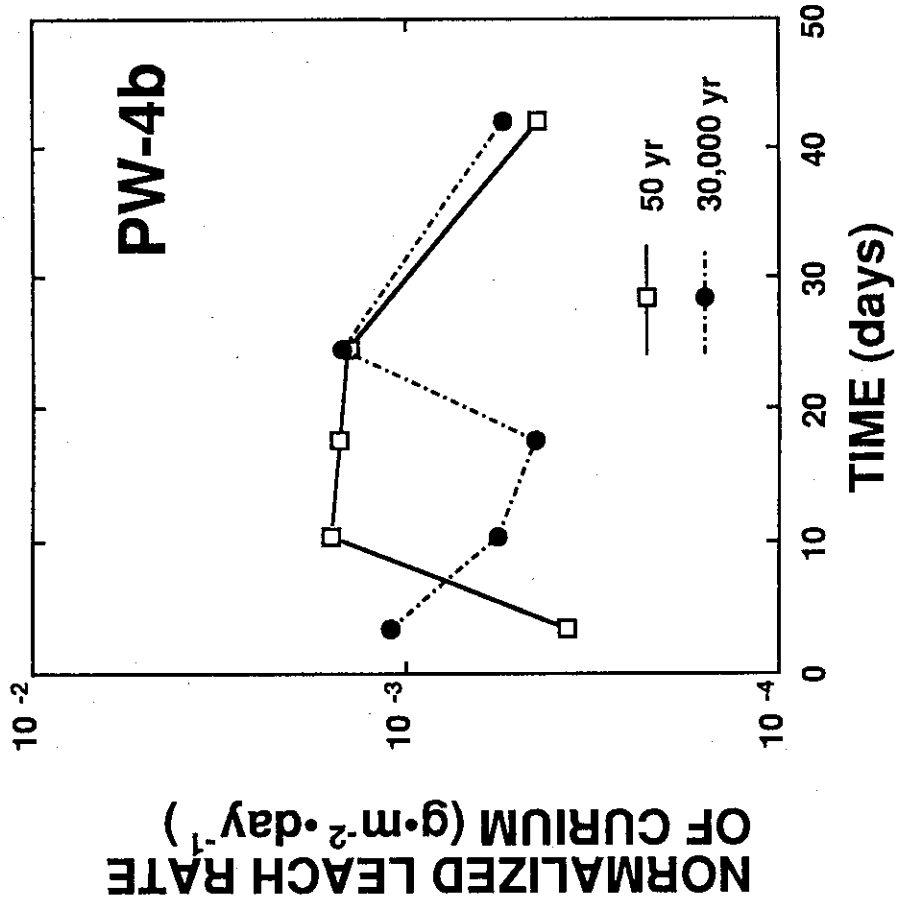

Fig. 3 Change in curium leach rate from 50-yr and 30,000-yr specimens versus leach time.

1.2.2 Durability of An $La_2Zr_2O_7$ Waste Form in Water

I. Hayakawa and H. Kamizono

Introduction

Zirconium is suitable as a major constituent of a TRU waste form because of the following three reasons. First, Zr-O bonds in a crystal have the bond energy of about 81 kcal/mole which is relatively high compared to other metal-oxygen bonds. Second, Zr forms an insoluble hydrate in a pH range of 1.7 to 10.5. Third, Zr oxides compounds with other metal cations tend to confine a considerable amount of actinide and lanthanide elements in their crystal structures.

In our previous work[1-3], $La_2Zr_2O_7$ with a pyrochlore structure showed good durability in water. As $La_2Zr_2O_7$ has a low leach rate, it is necessary to use powdered samples in order to increase their leachable surface areas. In the present study[4], we examine the effects of the particle size, leachant exchange method and stirring on the leach rates of each constituent, and then the durability of an $La_2Zr_2O_7$ waste form in various waters is determined.

Experimental

Nitrates of La and Zr were mixed with nitrates of simulated waste elements $Ce(NO_3)_3 6H_2O$, $Nd(NO_3)_3 6H_2O$ and $Sr(NO_3)_2$ at levels equal to 1.3 wt% CeO_2, 2.08 wt% Nd_2O_3, and 0.53 wt% SrO, respectively. The nitrates were dissolved simultaneously in 0.5 M HNO_3 to obtain a uniform solution. The solution was dried at 100°C and then calcined at 700°C to denitrate. The calcined powder was uniaxially pressed at 500 kg/cm^2 into pellets of 2 cm in diameter and 0.5 cm in thickness. These pellets were sintered at 1400°C for 16 h in air and ground to powders in a mortar. The powders were classified into the particle sizes of 125-250, 75-125, and <75 μm through the sieves.

We used the leachant exchange method described below to obtain the leach rates of each constituent. The classified powders were immersed in an HCl solution of pH=1.0, deionized water of pH=5.6 or an NaOH solution of pH=10 at 40°, 90° or 150°C. The powders were immersed for a given

period, and then the leachate was collected by decantation and fresh leachant was added. After leaching for about 4 days, the leachant was again collected by decantation. These operations were repeated. Part of the leachate collected by decantation was subjected to concentration measurements and the rest was filtered on a membrane of 0.45 or 0.025 μm. To examine the effect of stirring on leach rates, the leachate was stirred for about 10 seconds once a day and the results after the stirring were compared with those without stirring.

The acidity of the collected leachate was immediately adjusted to pH=1 with the addition of an HCl solution. Concentrations of elements in the acidified leachate were analyzed by inductively coupled plasma atomic emission spectroscopy (ICP) with mass spectroscopy (MS).

Results

Effects of the leaching method on leach rates

Based on preliminary experiments, the following three points are taken into account in the leach tests hereafter.

1. Classification of the particle size distribution is not necessary when the powders consist of fine crystal grains of less than 1 μm in diameter.
2. During leach experiments, stirring should not be applied.
3. The leachate should be filtered through a 0.45 μm membrane.

Effects of temperature and pH

Effects of leach temperature

The effects of temperature on the leach rates are shown in Figs. 1-3. The leach rates in Fig. 1 were obtained after immersion for 34 days in the acid solution. The leach rates of La, Nd, Ce and Sr increase slightly from 40° to 90°C and increase considerably from 90° to 150°C. The leach rates of La, Nd and Ce are almost the same as each other at 90° and 150°C. On the other hand, that of Zr decreases considerably from 40° to 90°C and decreases slightly from 90° to 150°C.

The leach rates in Fig. 2 were obtained by the leachant exchange method. This figure shows that the leach rates of La, Nd, Ce and Sr tend to increase with the increase of temperature as observed in Fig. 1. On the other hand, the leach rate of Zr at 90°C is almost the same as that at

40°C, and the leach rate of Zr at 150°C is lower than that at 90°C by one order of magnitude.

Figure 3 shows the effects of temperature on the leach rates in deionized water. The leach rates of Zr are lower than those in the acid solution at 40°C and 150°C. Two explanations are possible for this phenomenon. First, the increase of pH reduces the dissolution rate of $La_2Zr_2O_7$. Second, Zr forms an insoluble hydrate layer on the powder surface in a pH range of 1.7 to 10.5, which reduces the reaction rate of the inner part of the matrix in water.

Effects of pH in leachate

Figure 4 shows the effects of pH on leach rates. After samples were immersed in leachants at 90°C for 34 days, leachants were exchanged once in four days and the leach rates after 50 days were obtained. In the acid solution, the leach rate of each element decreases in the order of Sr > La ~ Nd ~ Ce > Zr. In deionized water and the alkaline solution, the leach rate of each element other than La decreases in the same order as in the acid solution. The leach rates of La in the alkaline solution are small in comparison with Nd and Ce. This small leach rate seems to be related to the formation of insoluble $La_2(CO_3)_3$.

Discussion

Effects of leach temperature

As shown in Fig. 1, the leach rates of Zr decrease with the increase of temperature in the acid solution. On the other hand, the leach rates of La, Nd, Ce increase with the increase of temperature. The following three points are possible causes for this phenomenon. First, the disintegration rate of the crystal lattice increases with increasing temperature. Second, solubility of constituents increases with increasing temperature. Third, the concentration of CO_3^{2-} in the leachate decreases with increasing temperature and this prohibits the formation of Zr-complexes with CO_3^{2-}. The increase of leach rates for La, Nd, Ce and Sr with increasing temperature (Fig. 1) is caused by the first and second effects described above. However, the decrease of leach rate of Zr with increasing temperature may be related to the third effect.

Effects of pH in leachate

The leach rate of Zr is smallest in deionized water. In the solution saturated with ZrO_2 at 25°C, the major ion species are $Zr_4(OH)_8^{8+}$(10^{-3} M) at pH=1, $Zr(OH)_8^-$ or $Zr(OH)_3^+$ (10 -12 M) at pH=5.6 and $Zr(OH)_8^-$ ($10^{-7.7}$ M) at pH=10. The concentration of Zr ions is small in a pH=5.6 solution. In our work, the concentrations of Zr in the leachates were 10^{-7} M at pH=1, $<10^{-8}$ M at pH=5.6 (deionized water) and 10^{-8} M at pH=10. The concentration of Zr measured at pH=10 was almost the same as that in the literature ($10^{-7.7}$ M), and this shows that Zr in the leachate may be saturated. However, the concentration of Zr measured at pH=1 was 10^{-7} M which is extremely low compared with the data in the literature (10^{-3} M) and it is thought that the low concentration of Zr is caused by the low dissociation rate of the $La_2Zr_2O_7$ crystal lattice.

Conclusions

The leach rates of an $La_2Zr_2O_7$ waste form, containing Nd, Ce and Sr as simulated waste elements, were measured at 40°, 90° or 150°C. The leach rates of each constituent in deionized water and an alkaline solution (pH=10) decreased more than one order of magnitude than those in an acid solution (pH=1). The leach rates of La, Nd, Ce and Sr tended to increase with increasing temperature. In contrast to this, the leach rate of Zr after immersion for 34 days decreased as temperature increased. This was attributed to the decrease of Zr-complexes with CO_3^{2-} ligands which are not stable at a higher temperature. The leach rates of Zr, La, Nd and Ce were less than 10^{-5} g $m^{-2}d^{-1}$ in deionized water and an alkaline solution (pH=10) at 90°C. This shows that $La_2Zr_2O_7$ can be a superior material for immobilizing transuranic elements.

References

1. I. HAYAKAWA and H. KAMIZONO, in Proceeding of the 3rd International Symposium on Advanced Nuclear Energy Research, Mito, March 1991 edited by JAERI p. 408.
2. H. KAMIZONO, I. HAYAKAWA and S. MURAOKA, J. Am. Ceram. Soc., 74 (1991) 863.

3. I. HAYAKAWA and H. KAMIZONO, presented at the 15th International Conference on Scientific Basis for Nuclear Waste Management, Strasbourg, France, on Nov. 5 in 1991.
4. I. HAYAKAWA and H. KAMIZONO, J. Mater. Sci., 28 (1993) 513.

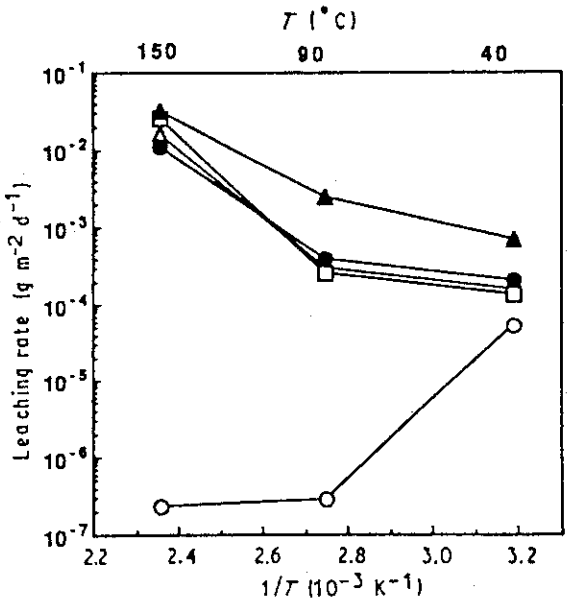

Fig. 1 Leaching rate after 34 days in an acid solution (pH=1). No exchange of leachant occurred. (○)Zr, (△)La, (□)Nd, (●)Ce, (▲)Sr.

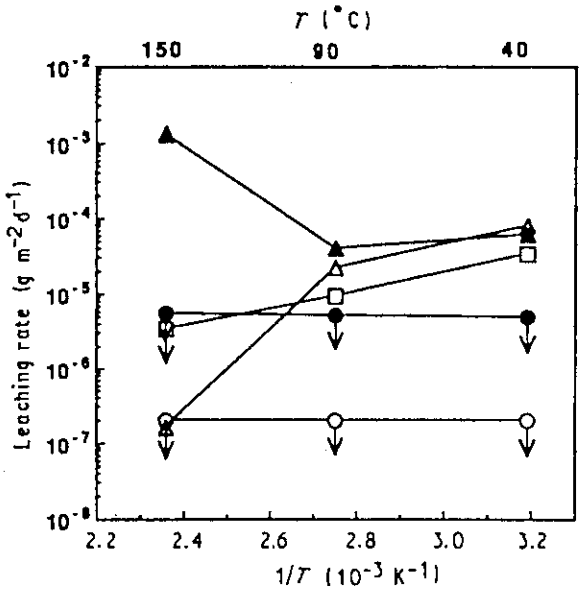

Fig. 3 Leaching rate after 50 days in deionized water. (○)Zr, (△)La, (□)Nd, (●)Ce, (▲)Sr.

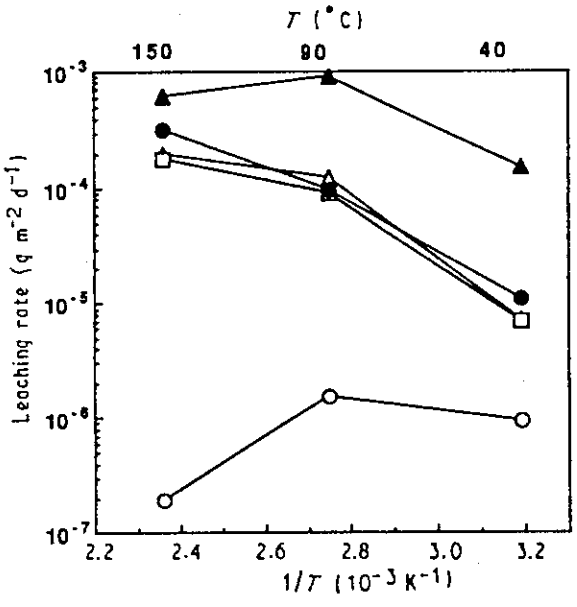

Fig. 2 Leaching rate after 50 days in an acid solution (pH=1). (○)Zr, (△)La, (□)Nd, (●)Ce, (▲)Sr.

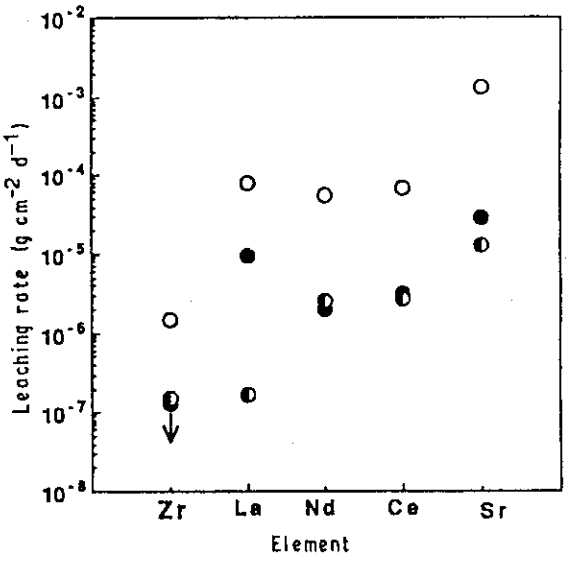

Fig. 4 Leaching rate of the constituent at 90°C after 50 days pH. (○)1, (●)5.6 and (◐)10.

1.3 Performance of Engineered Barrier Materials

1.3.1 Sorption Characteristics of Neptunium by Smectite

N. Kozai

Introduction

Sorption characteristics of neptunium by smectite (montmorillonite) which is one of the major clay minerals contained in bentonite (buffer material) have been studied by batch type experiment.

It is known that a difference in exchangeable cation of smectite causes the change of characteristics of smectite. Thus, sorption and desorption experiments were carried out using 4 types of smectite that had H^+, Li^+, Na^+ and K^+ as the exchangeable cation, respectively.

Experimental

Sorption experiments were carried out to discuss the relationship between pH of the neptunium solution and the amount of neptunium sorbed by smectite. Li-smectite, Na-smectite and K-smectite were prepared by substituting Li^+, Na^+ and K^+ for exchangeable cation of smectite, respectively. H-smectite was prepared by soaking Na-smectite in acid solution. Each smectite was added to the neptunium solution in polycarbonate centrifugation tube after the pH adjustment, and the mixture was kept at 20°C for 10 days. After the sorption experiment, the phase separation was carried out by centrifugation at 12000 rpm for 1 hr, and the pH and concentration of neptunium of the supernatant were measured.

Subsequently, desorption experiments using the sequential extraction procedure were carried out to clarify the association of neptunium with smectite. The smectite by which neptunium was sorbed was firstly treated with a 1 M KCl and secondly a 1 M HCl solution at 20°C. At the end of each extraction step, the suspended solution was separated by centrifugation mentioned above, and concentrations of the residual neptunium in the solid phases were measured after the residues were dissolved by a HF solution with heating.

Results

The Kd values of neptunium for smectite are shown in Fig. 1 as a function of pH of the solution. Figure 1 shows that the amount of neptunium sorbed by each smectite depends on pH of solutions and the exchangeable cation type of smectite.

Li-smectite (Fig. 1b) had the Kd values of neptunium between 20 and 100 $ml \cdot g^{-1}$, and the Kds did not depend much on pH of solutions in comparison with other types of smectite. The Kds by H-smectite (Fig. 1a) and K-smectite (Fig. 1d) increased with pH. And in case of Na-smectite (Fig. 1c), the highest Kd appeared at around pH 2.5, and the Kd decreased with increasing pH up to 5. The Kd showed a constant value of about 20 between pH 5 and 10, and increased with pH above 10.

However, the Kds by each smectite showed nearly the same value of about 20 between pH 6 to 7.

Percent fractions of neptunium desorbed from smectite are shown in Fig. 2. In all of the pH region, the neptunium adsorbed by each smectite was entirely desorbed with a 1 M KCl solution and a 1 M HCl solution. Figure 2 showed that the desorption behavior of neptunium from smectite depends on pH of solutions and the exchangeable cation of smectite. However, in the pH region of 6 to 7, most of the neptunium sorbed by each smectite was desorbed by KCl solution.

Therefore, the sorption-desorption behaviors of neptunium by smectite depends on pH of solutions and the exchangeable cation of smectite.

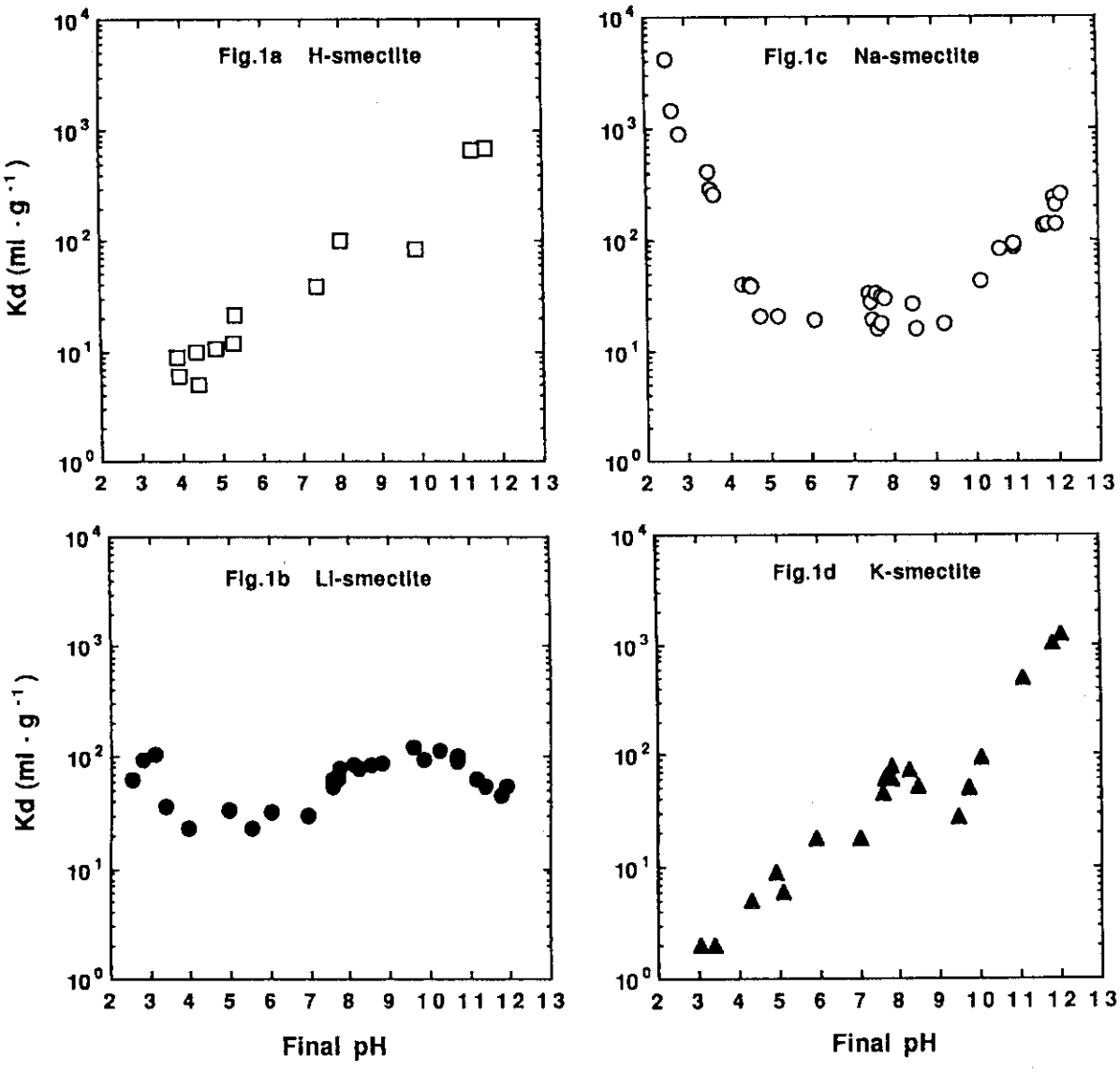

Fig. 1 Sorption behavior of Np by smectite.

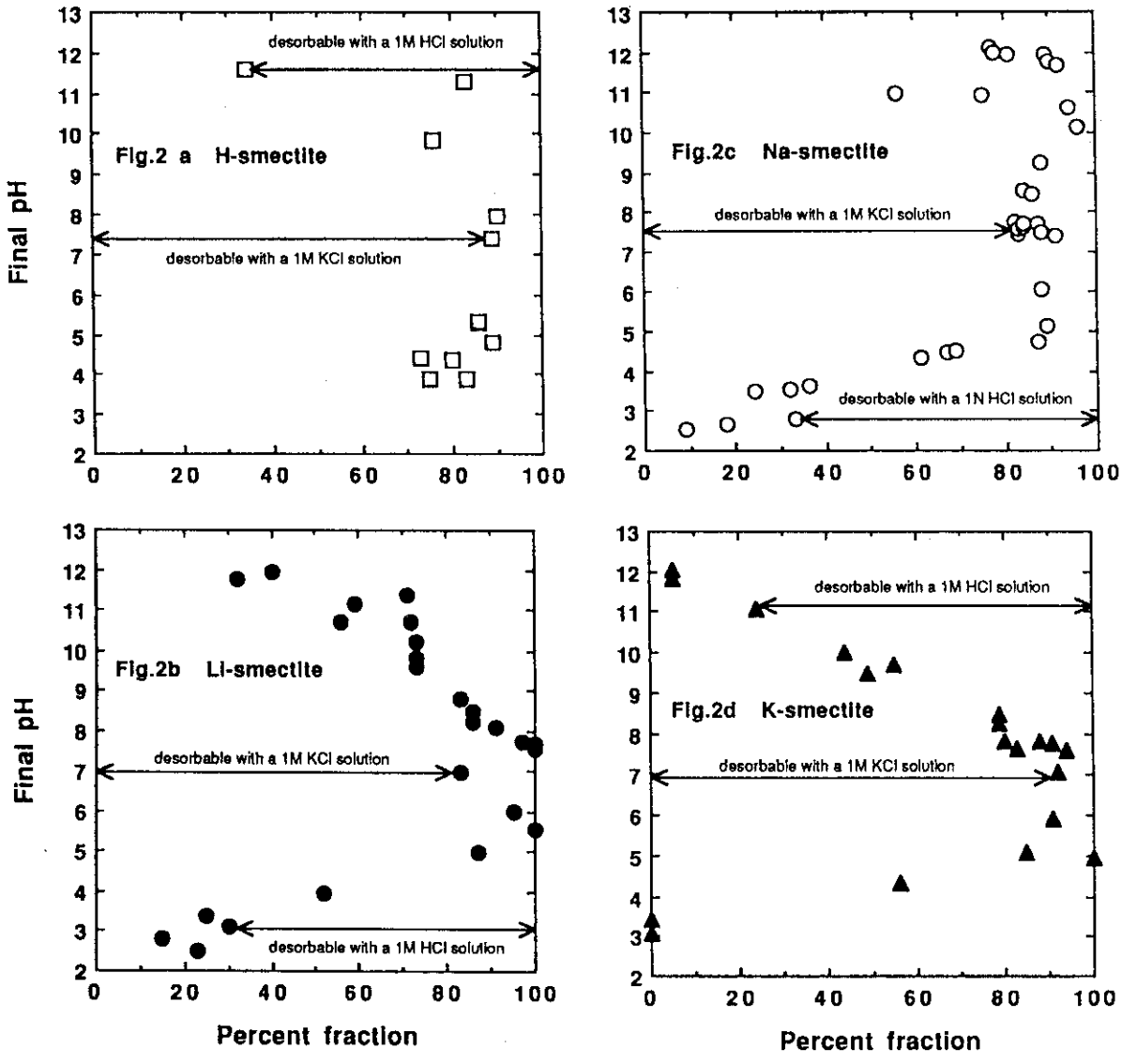

Fig. 2 Desorption behavior of Np from smectite.

2. Safety Evaluation Study for Geological Disposal

2.1 Behavior of Radionuclides in Underground Water

2.1.1 Effects of Temperature and pH on Crystallization Kinetics of Goethite from Ferrihydrite

T. Nagano

Effects of temperature and pH on crystallization kinetics of ferrihydrite to goethite were studied. Poorly ordered iron hydroxides were precipitated from 0.1M ferric nitrate solutions by adding 2M NaOH to pH11, 12.3, 13.1 and 13.8. Initial precipitates were identified as two-line ferrihydrite by X-ray diffractometry. Then the ferric gels were transferred into 12ml of transparent bottles and incubated at 40, 55, 70 and 85°C for each pH condition.

The goethite crystallization is accompanied with color variation from brown to yellow. In the previous work, the authors revealed that crystallinity of goethite was closely related to its color, especially b* value in the L*a*b* color space. Therefore the b* value was chosen as a kinetic parameter in this study. At selected intervals, color measurements on stored samples were conducted from bottoms of the bottles by using Minolta Chroma Meter, CR-200.

As a result, the b* values exponentially increase with the aging time. A crystallization reaction of goethite from ferrihydrite is known to follow a pseudo-first order reaction, indicating that a rate of the crystallization at any time is proportional to the amount of a residual ferrihydrite in the precipitate. The positive relationships between the goethite crystallinity and the b*-values mentioned above lead to an exponential increase in the b*-values. Consequently, the crystallization curves based on the b*-values are followed as an equation,

$$f = C_1 - C_2 \cdot \exp(-C_3 \cdot x) \qquad (1)$$

where f is the b*-value, x the incubation time, and C_1, C_2 and C_3 are constants. We can fit colorimetrical data to the equation (1) by a least-squares fitting method and determine a rate constant k (h^{-1}) of the overall reaction (C_3 in the equation (1)).

Temperature effects on the crystallization kinetics of goethite are given by Arrhenius plots for pH 13.1 and 13.8 (Figure 1), where only goethite was produced. A higher temperature results in a larger rate constant and a positive effect of temperature on the crystallization kinetics is obvious. The energies of activation of the overall reaction were calculated by slopes of the Arrhenius plots to be 10.15 Kcal/mol for pH13.1 and 9.92 Kcal/mol for pH13.8. These values lie in the range of most of the activation energies for a wide variety of mineral-solution alteration process such as dissolution of diopside, enstatite and augite. The most accepted model for the goethite crystallization consists of two different reactions, namely dissolution of ferrihydrite and reprecipitation of goethite. The result indicates that the dissolution of ferrihydrite is a rate determining step of the overall crystallization process.

Effects of pH on the crystallization kinetics are given by a diagram of logarithm of rate constants $k(h^{-1})$ against pH for various temperatures (Figure 2). At 40 and 55°C, a lower pH condition leads to a lower rate constant and a positive pH effect is obvious. According to a refined model, goethite is strongly favored where the concentration of monovalent Fe(III) ions such as $Fe(OH)_2^+$ or $Fe(OH)_4^-$ is at a maximum. In consideration of a fact that the $Fe(OH)_4^-$ ions is the most dominant species in high alkaline solutions beyond pH10, the $Fe(OH)_4^-$ ion is considered to be a dissolved form of ferrihydrite and an origin of reprecipitated goethite. Therefore, we can assume that the dissolution of ferrihydrite is a reaction between ferrihydrite and OH^-, namely OH^- promoted reaction. Based on this assumption, we can reasonably explain the positive effect of pH on the crystallization kinetics of goethite.

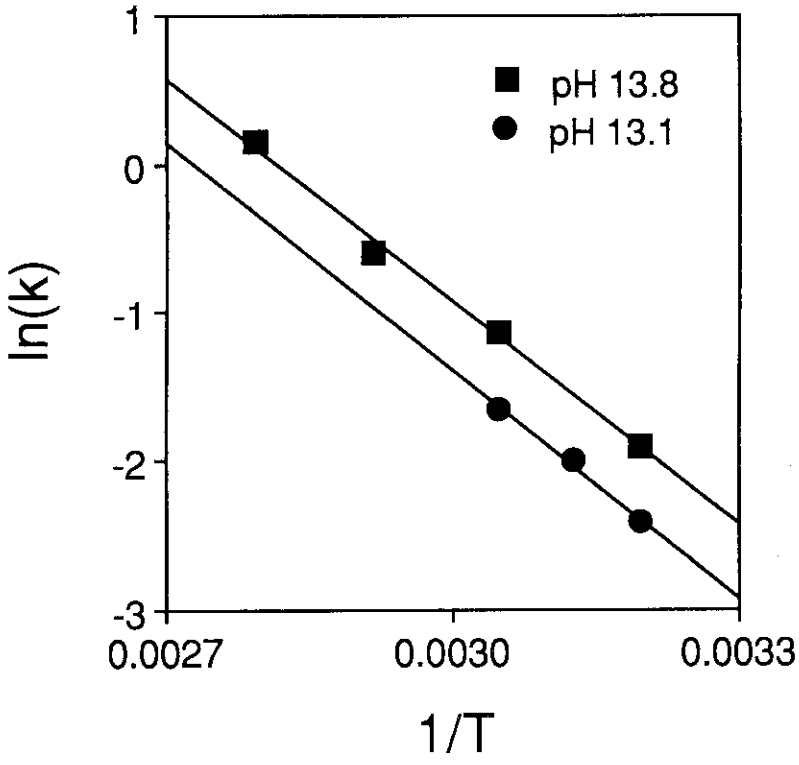

Fig. 1 Arrhenius plots for the goethite crystallization at pH 13.1 (40~55°C) and pH 13.8 (40~85°C).

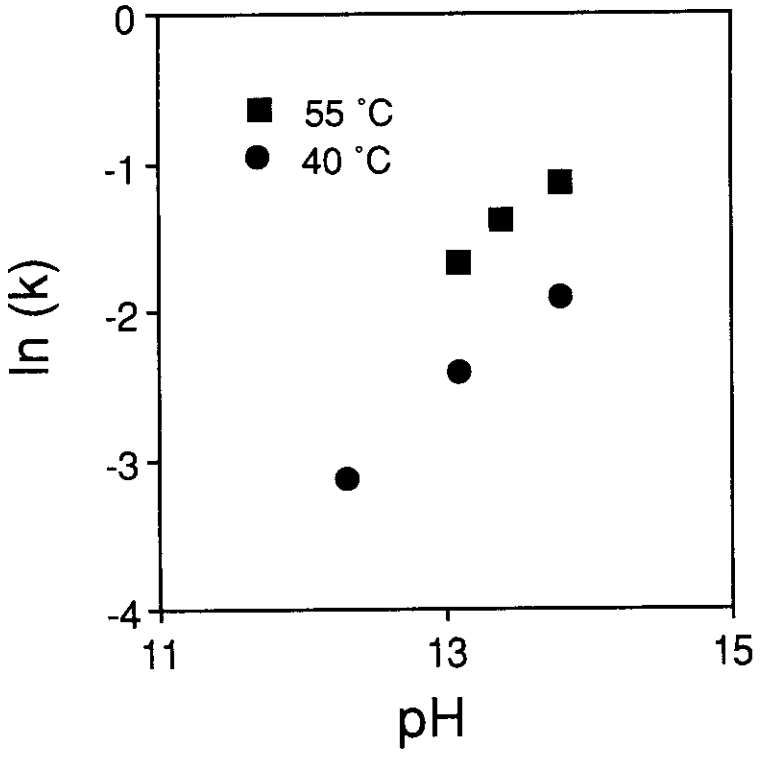

Fig. 2 Effects of pH on the crystallization rates of goethite at 40 and 55°C.

2.1.2 Diffusion of Strontium in Rock Matrix

T. Yamaguchi, Y. Sakamoto and M. Senoo

Introduction

After the high level radioactive waste is placed in a deep underground repository, radionuclides which escape from the engineered barrier may transport through the bed rock with ground water. The major fissure in the bed rock should be considered as a main transport path. It is recognized that the sorption onto rock surface and the diffusion into pore or micro fissure in the rock matrix are important factors retarding the transport of radionuclides. In order to evaluate the migration of radionuclides in deep geological formation, it is required to get a quantitative understanding of the diffusion of radionuclides in the rock matrix. In the present study, new data of Sr^{2+} diffusion were obtained and a possibility of the surface diffusion was discussed based on the theoretical formula giving an account of the surface diffusion.

Experimental

The rock used in this work was a biotite granite from Inada mine in Ibaraki prefecture. The original drilling cores of the granite were 40 mm in diameter and 300 mm in height. The cores were cut into circular plates having a thickness of 5 mm by a diamond cutter, and the pieces without visible fissure were used for the experiments. The porosity of the granite measured by a water saturation method was (0.68±0.03)% on an average of ten measurements. The pore size was distributed widely from 10 nm to 10 μm[1].

The diffusion cell and the method used in this study were almost the same as described in a previous paper[1]. Granite samples were pre-equilibrated for 30 days with 0.1M KCl solution, the pH of which were adjusted to 4. The reservoirs with a capacity of 116 ml were filled with 0.1M KCl solution. The pH of the solution was adjusted to 4 to prevent hydrolysis, precipitation of hydroxides and effects of carbonate. Diffusion experiments were started added into source reservoirs with tracers to get the concentration of 0.1M. The chemicals were of reagent grade from

Wako Pure Chemical Industry, LTD. The cells were kept at 25°C in a water bath. Two milliliters of the solution were taken from the sampling reservoir every three days at first and every ten days later. The concentrations of the tracers in the solutions were determined by inductively coupled plasma (ICP) emission spectrometry. Aliquots used for concentration measurements were replaced by an equal volume of 0.1M KCl solution to keep the balance of the water level of both reservoirs.

In a separate experiment, the diffusive behavior of strontium in the granite was also examined using deionized water in place of 0.1M KCl solution to make clear the effect of sorption on overall diffusive behavior. The concentration of strontium in the source reservoir was also 0.1M. No chemicals were added to the solution in this experiment in order to keep the ionic strength low, consequently, the pH of the solution was settled to 5.5. The experiment was triplicated at room temperature.

Results and Discussion

Diffusion of ions in a porous material is described as:

$$(\varepsilon + \rho R_d)\frac{\partial c}{\partial t} = D_e \frac{\partial^2 c}{\partial x^2} \qquad (1)$$

ε	porosity
ρ	density of the rock
R	distribution coefficient
$c(x,t)$	concentration of the ion in the solution
D_e	effective diffusion coefficient
x	length coordinate in the diffusion direction

The solution of equation (1) was given previously[2], the concentration of the sampling reservoir after a long period is approximated as:

$$c_2(t) = \frac{Alc_1}{V_2}\left\{\frac{D_e t}{l^2} - \frac{\alpha}{6}\right\} \qquad (2)$$

c_1	concentration in the source reservoir
c_2	concentration in the sampling reservoir
α	rock capacity factor $(\varepsilon + \rho R_d)$
l	thickness of the rock sample
A	cross section of the sample

V_2 volume of the reservoir

D_e and α are determined from the slope and the intercept on the concentration axis of the extrapolated linear region of a diffusion curve.

In 0.1M KCl solution, D_e and ρR_d are respectively $(2.7\pm0.6) \times 10^{-13}$ m^2/s and 0.006 ± 0.008 on an average of six measurements. In deionized water, they are respectively $(1.0\pm0.6) \times 10^{-11}$ m^2/s and 1.87 ± 0.39 on an average of three measurements. The sorptivity is much lower than in 0.1M KCl solution than in deionized water. In the presence of KCl, potassium ion may occupy sorption sites within the granite so that strontium is hardly sorbed. On the other hand, strontium may be present not only in the pore but also on the rock surface in deionized water. The difference in sorptivity may be mainly due to difference in ionic strength. The effective diffusion coefficient in deionized water was forty times larger than in 0.1M KCl solution. Although diffusion coefficients of ions in bulk solution become smaller at high ionic strength, the decrease may be at most thirty percents[3]. The difference in effective diffusion coefficients can not be explained only by the difference in ionic strength. Supposing that the sorbed strontium ions are mobile, the amount of mobile strontium ion within the granite is much larger in deionized water than in 0.1M KCl solution. The difference in D_e may be reduced into the difference in sorptivity. In the case that surface diffusion and pore diffusion contribute to the diffusion of sorbing species, diffusion equation can be described as

$$\varepsilon \frac{\partial c}{\partial t} + \rho \frac{\partial q}{\partial t} = D_p \varepsilon \frac{\partial^2 c}{\partial x^2} + D_s \rho \frac{\partial^2 q}{\partial x^2} \tag{3}$$

q amount of ion sorbed onto the rock

D_p pore diffusion coefficient

D_s surface diffusion coefficient

Since the relation between c and q is given by $q = R_d c$, equation (3) is simplified as:

$$\alpha \frac{\partial c}{\partial t} = (D_p \varepsilon + D_s \rho R_d) \frac{\partial^2 c}{\partial x^2} \tag{4}$$

Equation (4) is reduced into equation (1) if a different definition of D_e is made as:

$$D_e = D_p \varepsilon + D_s \rho R_d \tag{5}$$

The diffusion equation including surface diffusion is, thus, solved in the above mentioned way. In the case that surface diffusion is the predominant diffusion mechanism, the obtained D_e value is expected to depend on sorptivity, ρR_d according to equation (5). Figure 1 shows effective diffusion coefficients of strontium in several rocks as a function of sorptivity. The effective diffusion coefficient clearly depends on the sorptivity. The correlation between them seems to be divided into two parts, one of which is proportional at high sorptivity and another is independent at low sorptivity. In the case that sorptivity is high, diffusion of sorbed strontium may significantly affect the total diffusivity. In other words, the second term of the equation (5) may be dominant. In the case of low sorptivity, strontium may diffuse mainly through the pore hardly sorbed so that the effective diffusion coefficient of this part may be corresponding to the first term of the equation (5). The data can be well explained by taking pore and surface diffusion into account and expressed as:

$$D_e = 2.1 \times 10^{-13} + 3.5 \times 10^{-12}\ \rho R_d \qquad (6)$$

References

1. Nishiyama, K., et al.: Mining Geol., 40, 323 (1990) (in Japanese).
2. Crank, J.: "The mathematics of diffusion", 2nd ed. Oxford University Press, London, 50 (1975).
3. Mills, R.: Rev. Pure Appl. Chem., 11, 78 (1961).
4. Bradbury, M.H. and Stephen, I.G.: "Scientific Basis for Nuclear Waste Management IX", Materials Research Society, Pittsburgh, 81 (1986).
5. Lang, H., et al.: EUR-10121, 232 (1986).
6. Smith, P.A.: PSI-Bericht Nr. 53 (1989).
7. Bradbury, M.H., et al.: AERE-R 11995 (1986).
8. Skagius, K. and Neretnieks, I.: Water Resour. Res., 24, 75 (1988).

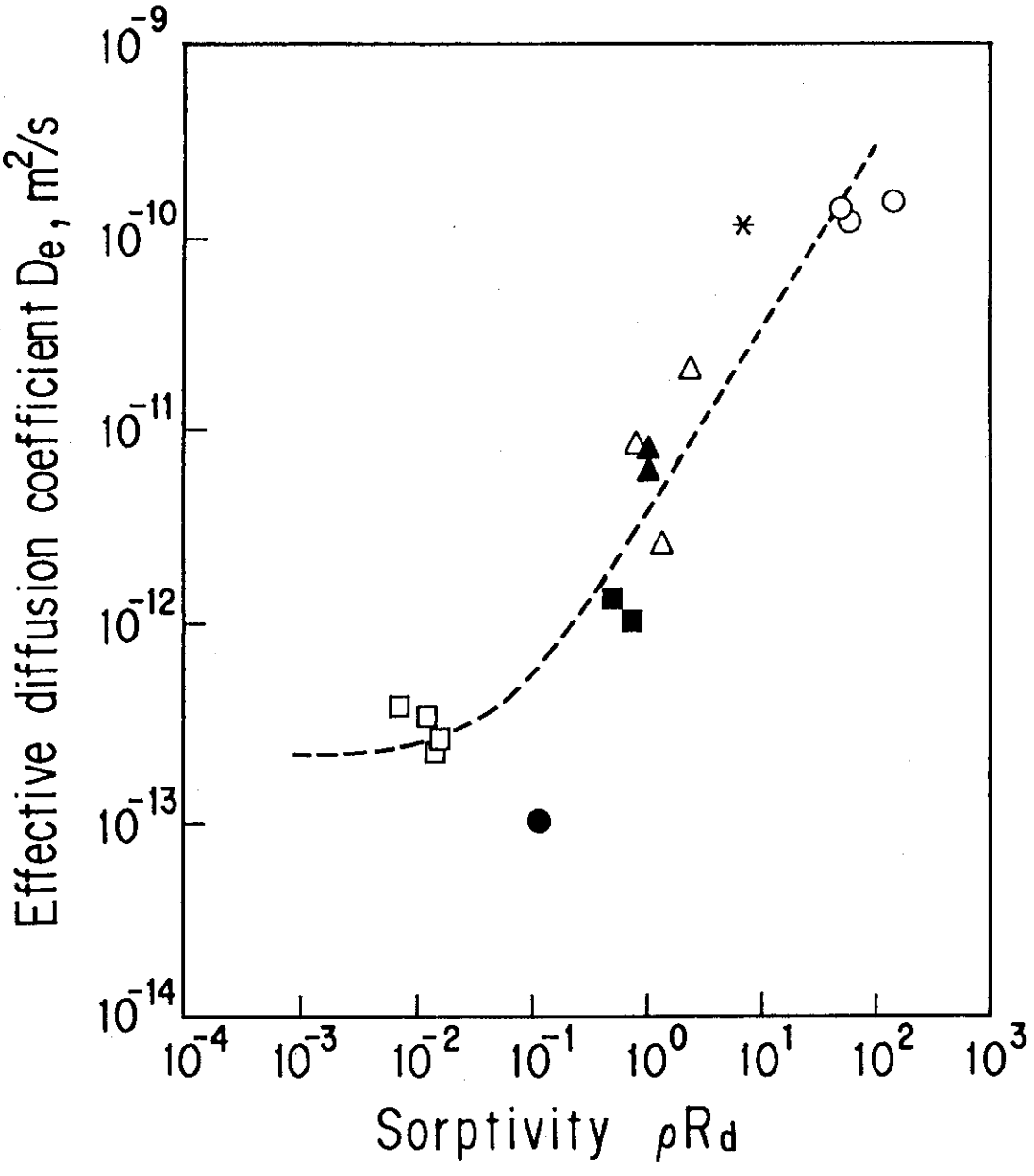

Fig. 1 Correlation between the effective diffusion coefficients of strontium and the sorptivities for several rocks. The line illustrates least square fitting of the data to the equation(5).

□ : Inada granite, in 0.1M KCl
△ : Inada granite, in deionized water
○ : Darley Dale sandstone[4,6]
＊ : cenomanian sample[5]
▲ : upper magnesian limestone[8]
■ : anhydryte[7]
● : biotite gneiss[8]

2.2 Radionuclide Migration Tests under In-situ Conditions

Prediction of the transport of radionuclides from waste disposal facilities requires an adequate understanding of the processes affecting the transport of specific radionuclides. To incorporate reality, experimentation aimed at predicting the transport of radionuclides should be made under in-situ conditions so that the geochemical and biochemical conditions of the system of interest should be accurately represented in the experimental system. For this purpose, several migration experiments were carried out under a JAERI/AECL cooperative program.

2.2.1 Migration Experiments under Deep Geological Conditions

M. Kumata

In the case of crystalline host rock for the high level radioactive waste, migration is expected to occur predominantly in existing, water-bearing fractures. These fractures are invariably coated with alteration minerals. To study the mobility of TRU elements under the geochemical conditions that exist at depth in crystalline rock, migration experiments have been performed under similar or in-situ conditions. An experimental system was designed to maintain the original geological conditions of the rock sample and the groundwater to be used in the experiments. The system was installed in an experimental room excavated especially for the program at the 240m level of the Underground Research Laboratory constructed Manitoba, Canada. Granitic rock sample for the migration experiments was taken from a fracture zone at a depth of about 250m.

The column experiments were performed with injections of ^{95m}Tc, ^{125}I, ^{237}Np, ^{238}Pu and ^{241}Am under deep geological conditions using groundwater from the fracture zone. The results obtained from the migration experiments showed that the experimental system could be used to maintain the original geochemical conditions of rock and groundwater in the fracture zone of granitic rock mass at the depth about 250m[1]. The bulk of the three injected actinides was strongly retained by the fracture filling materials in the column. However, small but significant fractions of the injected actinides were transported through the columns without retardation[2]. To study the effect of flow on radionuclide retardation, and to obtain information on the speciation of actinides that were transported

through the columns without retardation, further two sets of column experiment were planned. One was for neptunium and the other was for plutonium.

During last FY, ^{237}Np was injected into three columns at flow rate of 0.3, 1.0 and 3.0 ml/h in an anoxic chamber in the experimental room at the 240 m level of the URL. Eh, pH and electric conductivity of groundwater supplied to the column were monitored continuously before and during column operation. Materials used in this experiment were listed in Table 1.

Table 1 Materials used for neptunium migration test

Column	2.54 cm (ID) × 20 cm (L) stainless steel (surface was coated with Teflon)
Rock	crushed rock sampled from the fracture zone (180-850 μm fraction)
Water	groundwater from the fracture zone (unfiltered)
Nuclide	^{237}Np (2.7×10^{-5} mol/L), ^{3}H (123 Bq/ml)

Tritium was used as a non-reactive tracer and injected simultaneously with neptunium. After the injection of the tracer was completed, the flow was diverted around the accumulator and groundwater passed the column until the injected tritium was recovered. The groundwater was introduced into the columns from the fracture zone without contact air. The pressure of the groundwater supplied to the columns was limited to approximately 0.7 MPa by the specification of the solenoid valves to control the groundwater flow. To determine the speciation of the eluted ^{237}Np, a "speciation train" was connected to the outlet end of the column. The speciation train consists of holders for the two colloid filter membranes (pore size of 1000 nm and 50 nm), and columns for anion and cation exchange resins. The column operation record was listed in Table 2.

At the termination of the migration experiment, the speciation trains were removed from the columns and the 1000 nm and 50 nm filters were analyzed by gamma spectrometry. The anion and cation columns were also analyzed by gamma spectrometry for the presence of ^{237}Np. After that, the columns were removed from the anoxic chamber in the URL to recover the column material. The columns were frozen, and the frozen column materials were then sliced into 1 cm-long sections. These samples were dried and analyzed by gamma spectrometry.

Table 2 Column operation record

Column No.	Column Flow Rate (ml/h)	Injected Solution Volume(ml)	Column Operation Time(h)**	Total Eluted Volume From Column(ml)
1	0.3	30	384	115
2	1.0	30	107	107
3	3.0	30	35	105

* Neptunium spiked groundwater

** See text

Results and Discussion

Monitored values of pH, Eh and conductivity of the groundwater were shown in Fig. 1(a), (b). These results indicate the stability of the groundwater composition during the experimental period. No detectable ^{237}Np was found on any eluted solutions through the columns and speciation trains. This fact is indicating that the speciation train worked quite well to identify the chemical speciation of neptunium that passed through the column. Analytical results of the speciation trains were as follows; no detectable ^{237}Np was found on any of filters or on any of the cation exchange resins. Only the case of the flow rate of 3.0 ml/h, the highest flow rate, a very small amount (3.2×10^{-2} Bq) was found on the anion exchange resin. No activity was found on the other anion exchange resin. Almost all the neptunium injected into the columns was strongly retained within the columns. Distributions of neptunium in the columns were shown in Fig. 2. In the case of the flow rate of 0.3 and 1.0 ml/h, neptunium retained in the column was restricted three or four centimeters from the column inlet. Only the case of flow rate of 3.0 ml/h, neptunium was distributed in a hole column and this suggested that some neptunium was passed through the column. These results were well agreed with the results of eluent analysis. From the experimental results it would be able to conclude that all injected neptunium reacted with mineral on their surfaces (no non-react portion passed through the column) and reaction time is somewhat necessary to retain neptunium on the mineral surfaces and not enough in the case of the flow rate 3.0 ml/h.

References

1. Kumata, M. and Vandergraaf, T.T.: "Nuclides Migration Tests Under Deep Geological Conditions", Proc. 3rd Int. Symp. on Advanced Nuclear Energy Research, pp. 414-419, 1991.
2. Kumata, M. and Vandergraaf, T.T.: "Migration behaviour of long-lived radionuclides under deep geological conditions", 29th Int. Geological Congress, 24 August-3 September, Kyoto, Japan, 1992.

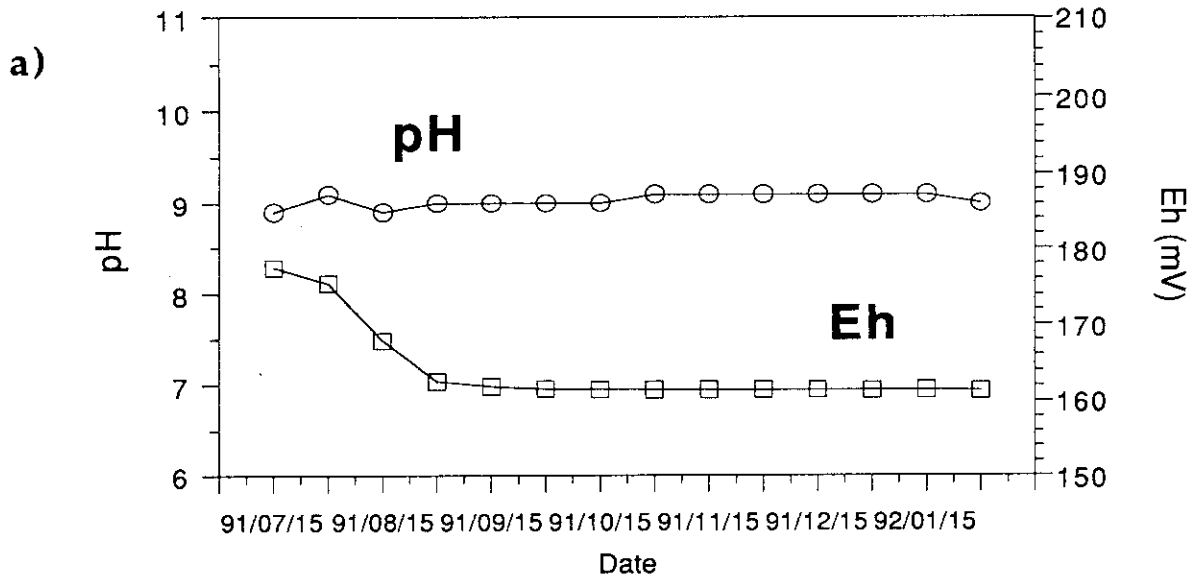

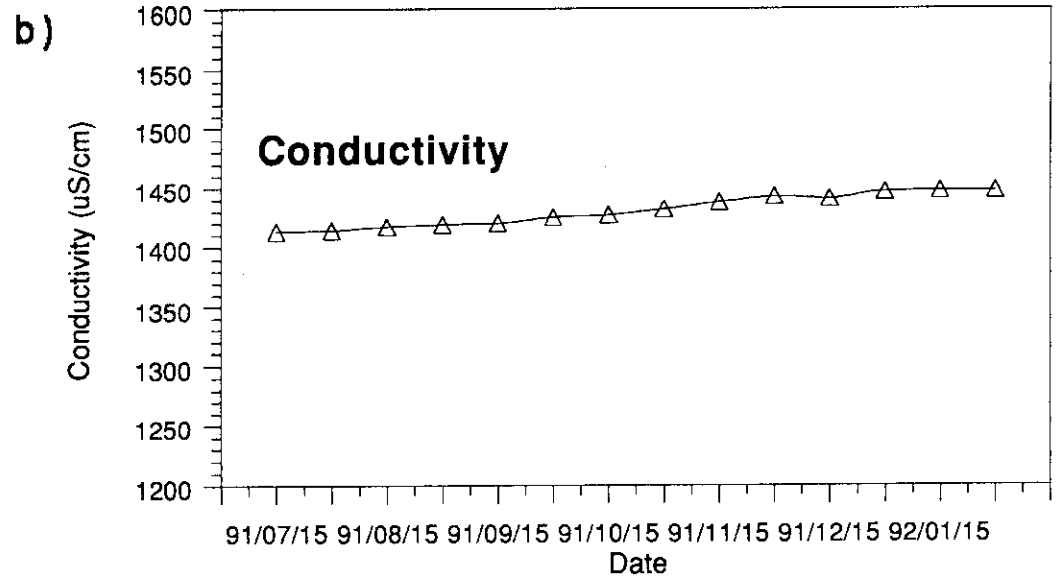

Fig. 1 Monitored results of a) pH, Eh and b) conductivity of the groundwater in the TK-1 tank

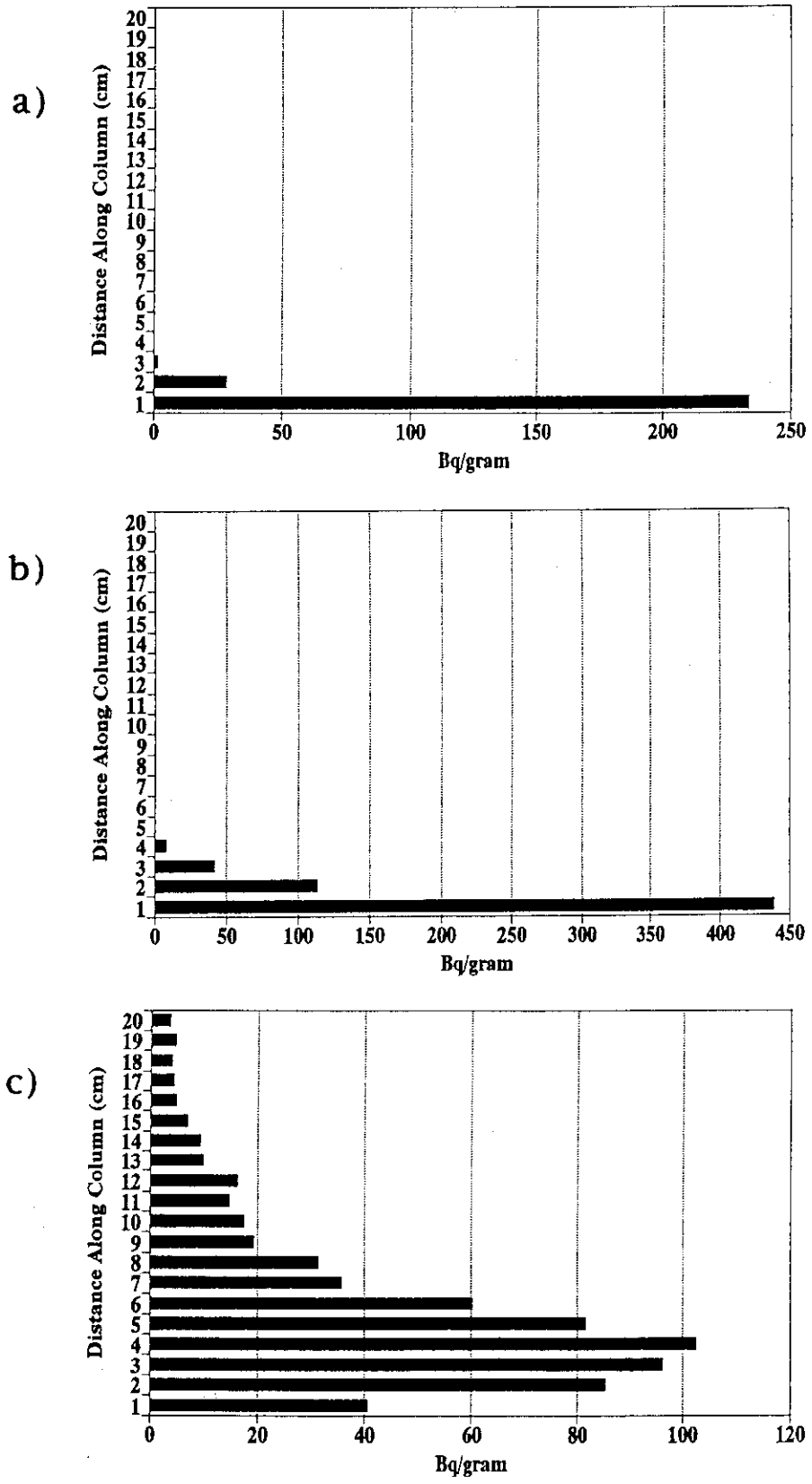

Fig. 2 Neptunium distribution profiles in the column a) No.1 (flow rate 0.3 ml/h), b) No.2 (flow rate 1.0 ml/h) and c) No.3 (flow rate 3.0 ml/h)

2.2.2 Glass Block Site Experiment

Y. Sakamoto

Introduction

In 1960, 25 glass blocks (a nominal weight: 2 kg/block) including radionuclides listed in Table 1[1] were buried in the aquifer sand at the Chalk River Laboratories (Atomic Energy of Canada Limited). The radionuclides have leached into groundwater from the glass blocks and have spread in the aquifer sand for 31 years. Under the cooperation between JAERI and AECL, migration behavior of radionuclides under the in-situ condition is being investigated from 1990. The plume mappings of ^{90}Sr and ^{137}Cs on sand have already completed till 1991. Now, we are challenging to get a mapping of actinide element. To study the sorption form of radionuclides on the aquifer sand, a sequential extraction technique was applied. The extraction of ^{90}Sr has finished and one of ^{137}Cs is in progress. Speciation test of the radionuclides in groundwater was carried out with using a large volume sampling column that cation exchange resin, anion exchange resin and alumina were embedded. The current results were summarized in this report.

Experiment

Plume mapping

The sand samples were taken at 0.25-10 m horizontal intervals from the glass blocks, and at 15 cm vertical intervals in a piston sampler to get the spatial distribution of the radionuclides. The sands were leached twice with a hot aqua regia solution, taken to dryness, and re-dissolved in 1N nitric acid. Radioactivity of ^{90}Sr was measured by Cerenkov counting using a liquid scintillation counter, and one of ^{137}Cs was analyzed by a gamma counting. The measurement results were used to draw the plume of the radionuclides.

Sequential extraction

The radionuclides on sand were divided to four adsorptive forms with four steps sequential extraction; ion exchange form, sorbed on amorphous

Fe-oxide, sorbed on crystalline Fe-oxide and fixed (residual). The ion exchange form was defined as a fraction to be extracted by 1M $MgCl_2$ solution, the amorphous Fe-oxide form as a fraction to be extracted with 0.25M NH_2OH-0.25M HCl solution and the crystalline Fe-oxide form as a fraction to be extracted with 0.3M sodium citrate, 1M $NaHCO_3$ and $Na_2S_2O_4$.

Speciation test

To investigate chemical form of the radionuclide in groundwater, speciation test was carried out with a large volume sampling column. This column has 0.45 μm filter, cation exchange resin bed, anion exchange resin bed and alumina bed. The radionuclides are trapped into each bed corresponding to the electrical charge of them. The particulate is trapped on the filter and neutral one in the alumina bed. The groundwater was sampled at the 1, 5 and 10 m downgradient of the glass blocks from a piezometer. Total sampling volume of groundwater was determined by flow rate and cumulative sampling time. The radionuclides onto each bed were leached into 1N· HNO_3 solution and their radioactivities were analyzed by gamma-ray spectroscopy.

Result and Discussion

The characteristics of sediments and groundwater were tabulated in Table 2 and 3. The cross section of the burial site along groundwater flow direction and a plume of ^{90}Sr were illustrated in Fig. 1. ^{90}Sr was found only in the medium fine sand layer sandwiched by two slit layers. This is because that groundwater flow in vertical direction is less, since hydraulic conductivity of slit layer is much lower than one of medium fine sand layer. Figure 2 shows depth averaged plumes of ^{90}Sr and ^{137}Cs on sand. A front of ^{90}Sr plume achieved to about 75 m from the glass blocks for 31 years. Distribution coefficient (K_d value) which was calculated from the rate of plume front advance was 5.5 ml/g. On the other hand, the K_d value from the laboratory batch test using the glass block site's sand was 7.5 ml/g. These values were approximately agreement each other. This fact implies that a part of migration behavior of strontium can be evaluated from experiment's result in laboratory, according to K_d model. Figure 3 shows result of sequential extraction. About 70% of strontium was extracted as the ion exchangeable cation. This result supports that most of

strontium migration is based on simple cation exchange corresponding to K_d model. On the other hand, 25% of strontium associated with amorphous iron oxide. According to Melnyk et al., a kinetic sorption-desorption reaction of strontium with iron oxide[2] plays an important role in the strontium migration in aquifer sand layer. Then, the result in Fig. 3 supports the probability of strontium kinetic sorption reaction with amorphous Fe-oxide.

A cesium plume front achieved to only 4 m for 31 years. The result of sequential extraction in Fig. 3(b)[3] suggested that fixation of cesium into sand and association with iron oxide controls the cesium adsorption behavior. The cesium incorporation into minerals like mica has been reported[4,5], and this observation is agreement with the result in Fig. 3. Then, it is likely that ^{137}Cs exists only around the glass blocks by fixation or strong adsorption onto sand.

Figure 4 shows the result of speciation test. Most of chemical form of ^{241}Am was cationic one for all sampling points. From a calculation using geochemical code MINTEQ, chemical forms of americium were Am^{3+} (87.2%), $AmOH^{2+}$ (9.2%) and $AmCO_3^+$ (3.5%) under the chemical condition as shown in Table 3. This result presents that most of americium is estimated as cationic ion in groundwater, and it was agreement with the observed data. Although it is not clear whether the calculated chemical form directly corresponds to real chemical forms, we can say that this calculation result with using thermodynamic data supports the observed data in Fig. 4. In the case of cesium, most the of chemical form was particulate at 1 m point. At other points, however, cationic form was main one. Because the existence of microbiological particulate form of cesium at the glass block site was reported by Champ et al. in 1981[6], it is probably that the particulate form found at this time is maybe same one. Furthermore, this particulate maybe be filtrated by sand layer to be found only at 1 m point from glass blocks.

References

1. R.W.D. Killey et al., The glass blocks site radionuclide migration study-data base review and current studies, Proceeding of transport and mass exchange processes in sand gravel aquifers: Field and modelling studies, Vol.2, 850 (1990).

2. T.W. Melnyk, F.B. Walton and L.H. Johnson, High-level waste glass field burial test: Leaching and migration of fission products, Nucl. Chem. Waste Management, Vol. 5, 49 (1984).
3. R.E. Jackson and K.J. Inch, Radionuclide Adsorption in Hydrogeochemical Processes Affecting the Migration of Radionuclides in a Fluvial Aquifer at the Chalk River Nuclear Laboratories, Sci. Series No.4, Inland Waters Directrorate, Environmental Canada, Ottawa, 41 (1980).
4. C.W. Francis and F.S. Brinkley, Preferential adsorption of ^{137}Cs to micaceous minerals in contaminated fresh water sediment, Nature, 260, 511 (1976).
5. K.E. Lyon and R.J. Patterson, Retention of ^{137}Cs and ^{90}Sr by mineral sorbents surrounding vitrified nuclear waste, NHRI paper No.27 (1985).
6. D.R. Champ and W.F. Merritt, Particulate transport of cesium in grondwater, AECL-7440 (1981).

Table 1 Radionuclide inventory

Radionuclides	Concentration (MBq/g)	Total (GBq)
^{137}Cs	158	7900
^{90}Sr	42	2100
^{241}Am	0.33	16.5
^{154}Eu	0.083	4.2
^{239}Pu	0.019	0.095

Radioactivity is corrected to 1991's value.

Table 2 Characteristics of sediments

Mineralogy	Granitic(fine sand)
Mean grain size	0.175 mm
Porosity	0.38
Hydraulic conductivity	4 to 8 m/day
Linear average velocity	0.17 m/day

Table 3 Characteristics of groundwater

Dissolved ion and other parameters	Concentration
pH	5.7
Eh	420 mV
DO	0.3 to 3 ppm
Ca^{2+}	5
Na^{+}	2 to 4
HCO_{3-}	10 to 15
SO_4^{2-}	15 to 18

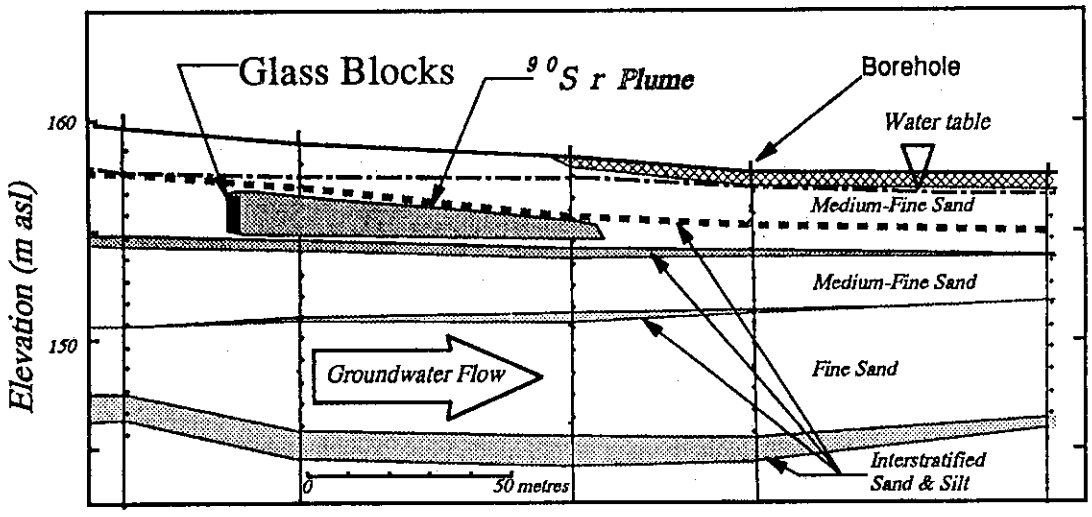

Fig. 1 Stratigraphic section along the groundwater flowpath

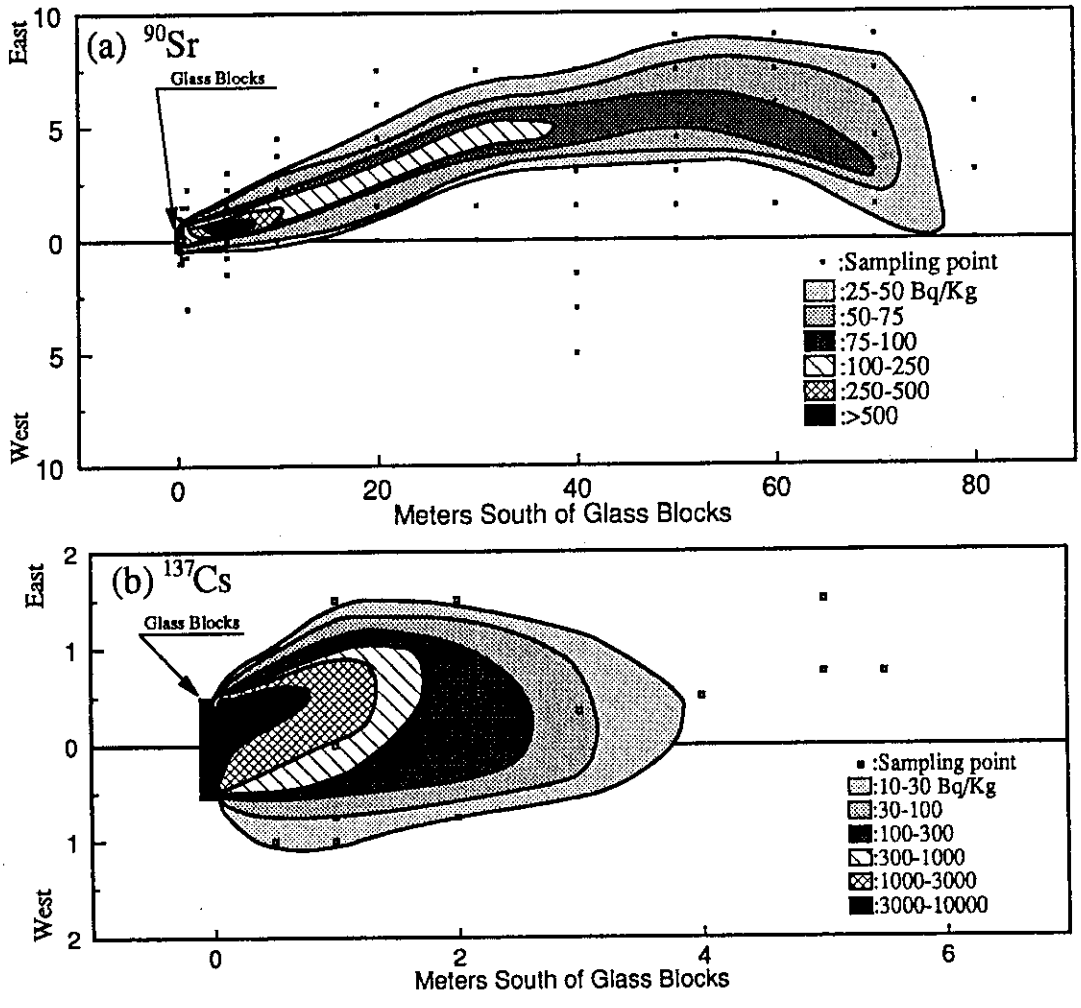

Fig. 2 Plume of depth averaged ^{90}Sr and ^{137}Cs on sand

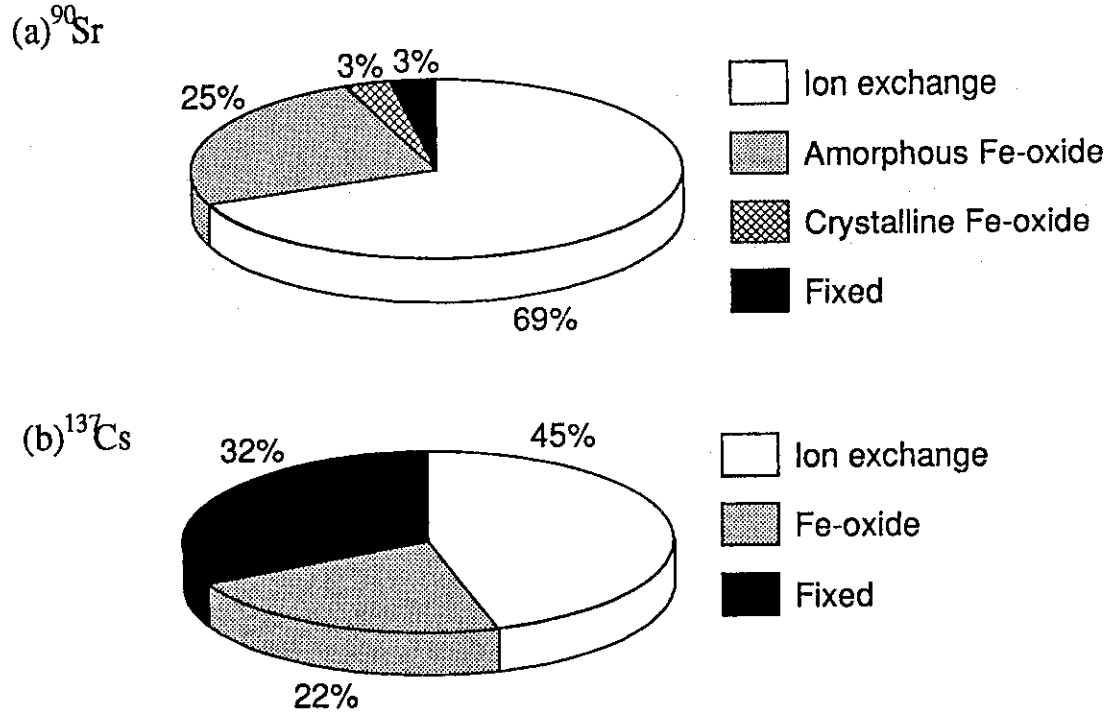

Fig. 3 Strontium and cesium fractions in the sequential extraction of sand (a) 5.5m South, 0.75m East (b) Data from ref.(3)

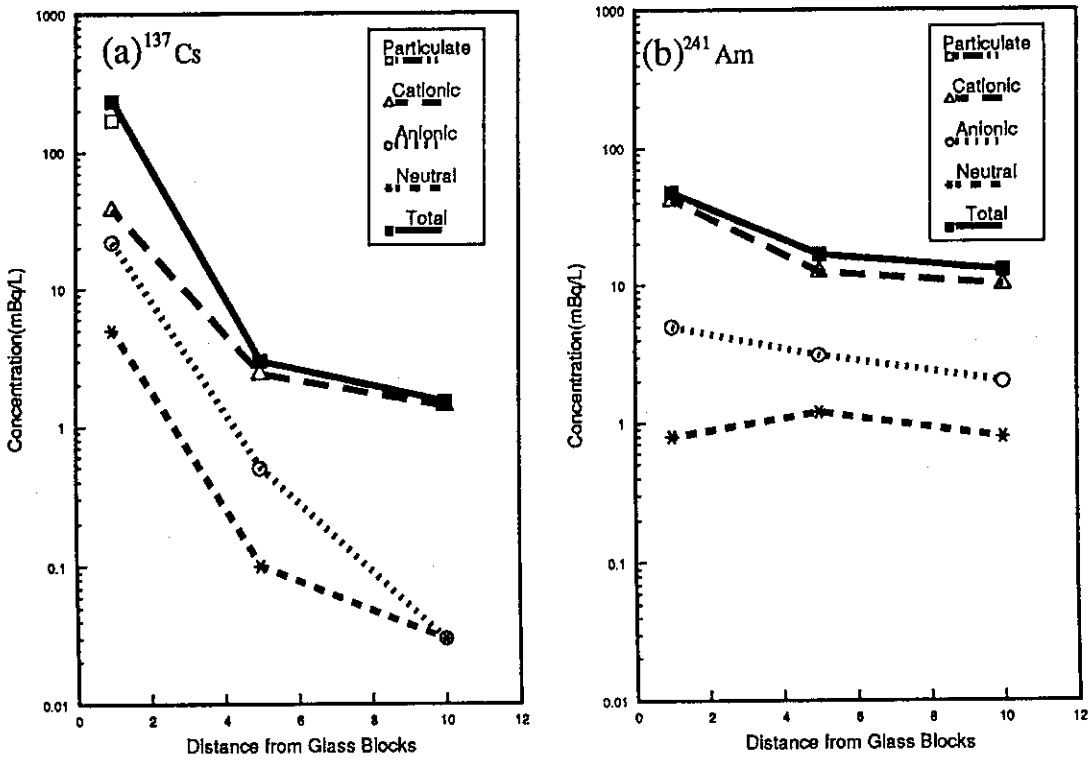

Fig. 4 Cesium and americium concentration in groundwater

2.3 Study on Natural Groundwater Flow System

M. Kumata

Groundwater flow is a key of the radionuclide migration at underground. For the long term safety assessment of the underground disposal of the HLW, it should be well known that groundwater flow system around the vault. Stable isotope hydrology using deuterium and oxygen-18 contained in natural groundwater is considered as a useful technique for investigation of the long term groundwater movement. To study the stable isotope hydrology, an analytical technique using mass spectrometor is being prepared and pretreatment methods of groundwater to measure the mass ratios of $^{2}H/^{3}H$ were examined. An area was selected for the stable isotope hydrology in Japan and the groundwater was sampled from the area.

In the case of hard rock as a host rock of the HLW vault, fractures play an important role in the groundwater hydrology. Geotomography, the application of medical computed tomography to the underground survey, is one of the most effective technique to estimate rock fractures. Fundamental study of geotomography was started last year. Electrical profiling was performed in JAERI property to study basics of resistivity (geo-) tomography[1,2].

References

1. Kumata, M. and Chiba, A.: "An experimental study on electrical profiling by using an intelligent measuring equipment for multi-stations", Proc. 86th SEGJ Conf., pp. 365-369, 1992 (in Japanese).
2. Kumata, M. and Chiba, A.: "A consideration of the influence of the contact resistance on the apparent resistivity of geoelectrical profiling", Proc. 87th SEGJ Conf., pp. 177-182, 1992 (in Japanese).

3. Natural Analogue Study

3.1 Changes in Layer Charge of Smectites and Smectite Layers of Illite/Smectite in Diagenetic Alteration

T. Sato, T. Murakami, T. Ohnuki and H. Isobe

Introduction

The use of smectites a major component for backfill barriers and seals in radioactive waste repositories is based on a permeabilty barrier (swelling property) and an adsorbent (high cation-exchange capacity) of transuranic ions and fission products. Of great concern is the conversion of smectite to illite or chlorite (non-swelling phase) that have been observed in natural settings (burial diagenesis, hydrothermal alterations, and low-grade metamorphism) and laboratory experiments. The formation of illite would lessen the barrier's performance due to a reduction in swelling properties and decreased cation-exchange capacity.

On the other hand, the smectite-illite group of clay minerals account for 30% of the mass of the Earth's sedimentary cover[1]. This enormous mass explains the significant role of this mineral group in the cycle of materials at earth's surface environment. Several studies have emphasized that the water dehydrated during smectite to illite conversion contributes to the migration of some materials (e.g., hydrocarbon and silica).

The major problem that needs to be resolved, both for geotechnical use such as repository design and for a clearer understanding of the material cycle at earth's surface environment, is the mechanism of smectite to illite conversion. The conversion results from an increase in the net negative charge on the smectite layers. Once the net layer charge is sufficiently large and then it is followed by the potassium fixation and interlayer collapse. Thus, it is the key to know how the layer charge is created to understand the mechanism of smectite to illite conversion. The aim of the present study was to elucidate the changes in amount and location of layer charge of smectites and smectite layers of I/S in diagenetic process.

Materials and Experimentals

Samples used for the present study were collected from Tertiary sandstones and shales exposed along the Nakanomata and Yachi river in Niigata, Japan. The sandstones and shales were formed by diagenetic alteration[2].

To obtain the clay fraction, the sandstones and shales were ground, ultrasonified, and separated by centrifugation. The clay fractions were, before X-ray diffractions, treated by (1) ethylene glycol solvation, (2) K-saturation and ethylene glycol solvation, (3) Li-saturation, heating at 250°C for 24 hr, and glycerol solvation (Greene-Kelly test), and (4) alkylammonium ion saturation. These treatments were carried out to estimate (1) percentage of smectite layers, (2) layer charge of expandable layers, (3) percentage of beidellite layers, and (4) mean layer charge, respectively. Mean layer charge was estimated according to the convenient method presented by Olis et al. (1990)[3].

Results and Discussion

The variation of the percentage of smectite layer in illite/smectite interstratified minerals (hereafter, I/S) is shown as a function of stratigraphic depth in Fig. 1. The percentage of smectite layers in I/S decreases continuously from 100% to 30% with stratigraphic depth. This decrease is accompanied by the structural change from the random to ordered interstratification. Between the random and ordered structures, a mixture of the two types of ordering is observed.

Figure 2 shows X-ray diffraction patterns after Greene-Kelly test, the sampling positions, percentages of smectite layer, mean layer charge for smectite samples, and percentages of beidellite layer for I/S. The pattern of smectite of the younger sediment (NB39M) shows a spacing of 9.5Å, and most of the layers of this sample have montmorillonitic character (octahedrally charged). On the other hand, the pattern of smectite just before illitization (KA05S) shows a spacing of 17.8Å, and most of the smectite layers of this sample have beidellitic character (tetrahedrally charged). Greene-Kelly tests have revealed that smectite precursors are montmorillonitic, and some of the montmorillonite layers of the precursors change into beidellite layers with increasing depth before illitization. This suggests the increase of charge is due to Al for Si substitution in

tetrahedral sheets before illitization.

At the early stage of illitization, the amount of the beidellite layers showed by not-shadowed peak decreases with increasing that of illite layers in I/S (Fig. 2). This decrease indicates the conversion of beidellite to illite layer occurs preferably. In addition to these changes, the smectite layers in I/S are converted to high charged layers for the samples with K and EG saturation. The increase of the layer charge in this study is mainly due to the substitution Al for Si, because, as mentioned above, the substitution continuously occurs before illitization.

The results of the EG solvation tests suggest that there exists an intermediate stage in the conversion process from g=0 to g=1, where the segregated structure with random and ordered I/S is dominant. The ordered I/S appear after the disappearance of the reflections of the beidellite layers. This suggests that the contribution of the beidellite layers to the formation of the ordered I/S is more effective than that of the montmorillonite layers.

Conclusion

In this diagenetic alteration, the beidellitization occurs with increasing layer charge and increasing tetrahedral charge before illitization. The continuous increases of the layer charges are due to solid-state Al for Si substitutions. The substitution may continue after illitization, because the layer charge of smectite layers in I/S continuously increase. In early illitization, the conversion of precursor beidellite to illite occurs, preferable, because percentages of beidellite layer immediately decrease after illitization. Moreover, the precursor beidellite may be contributed to form the ordered I/S. Thus, the charge characteristics of precursor smectite affect the reaction pathways of the smectite to illite conversion. We believe diagenetic processes inferrred for this area are applicable to other geologically similar settings, i.e., where shales are rich in I/S.

References

1. Carrels, R.M. and Mackenzie, F.T. (1971) Evolution of Sedimentary

Rocks: W.W. Norton, New York.

2. Sato, T. and Watanabe, T. (1989) Diagenetic alteration of Neogene sedimentary rocks in the No district, Niigata Prefecture: Jour. Jap. Assoc. Miner. Petrol. Econ. Geol., 84, 259-269.
3. Olis, A.C., Malla, P.B. and Douglas, L.A. (1990) The rapid estimation of the layer charges of 2:1 expanding clays from a single alkyl-ammonium ion expansion: Clay Miner., 25, 39-50.

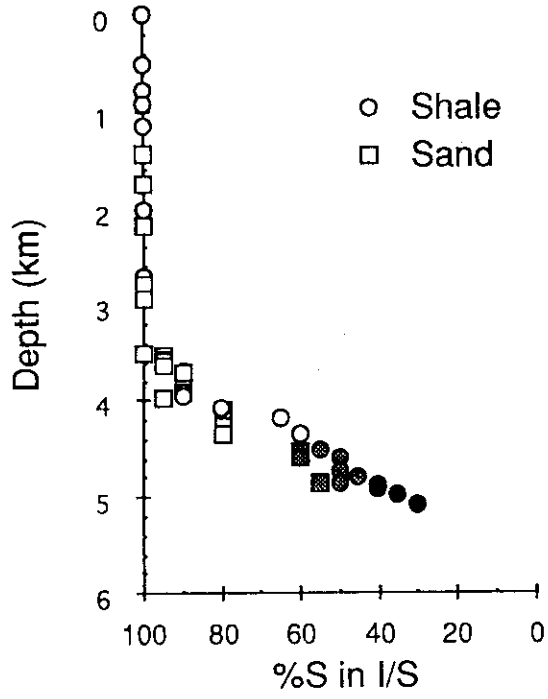

Fig. 1 Variation in smectite percentage of I/S with geological depth. Open symbols= random interstratification; solid symbols=ordered interstratification, shadowed symbols=mixture of random and ordered interstratifications.

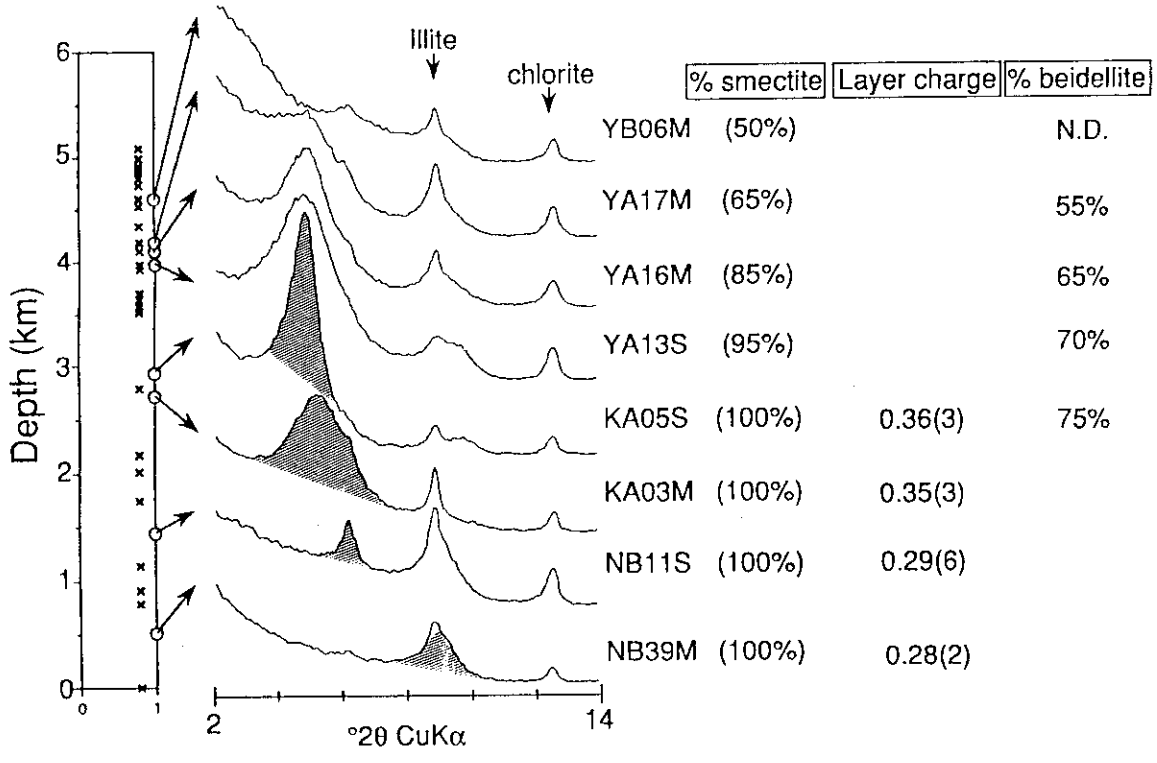

Fig. 2 X-ray diffraction patterns of Li-saturated samples after heating and glycerol solvation, their sampling positions, percent smectite layer, mean layer charge, and percent beidelite layer.

3.2 Alteration of Uranium Minerals in the Unweathered Zone

H. Isobe and T. Murakami

Introduction

Uranium deposits are the result of the alteration/dispersion, transportation and concentration of uranium in the Earth's near surface over geologic periods of time. The natural mineral assemblage of a uranium deposit is at least a partial record of these diverse processes. Natural analogue studies are carried out on natural uranium deposits to understand migration processes of elements[1,2,3]. In a well-constrained geochemical environment, one may use the alteration and paragenesis of the mineral phases as an analogue to the possible long-term behavior of radionuclides in spent fuel exposed to similar relevant conditions[1,4].

On the Koongarra uranium deposit, Australia, Snelling[5] described the zoned structure of the ore body and proposed reaction paths for the alteration of the primary uraninite to the formation of uranyl silicates. The minerals of the primary ore zone are uraninite with U-Pb oxides and uranyl silicates. Snelling concluded that the final alteration products of the unweathered zone were the sklodowskite-uranophane series ((Mg,Ca) $Si_2U_2O_{11}\cdot 6\text{-}7H_2O$). His diagram shows two main paths from uraninite to the sklodowskite. One sequence was through uranyl lead oxides such as curite ($Pb_3U_8O_{27}\cdot 5H_2O$). The other sequence was direct formation of the uranyl silicates from uraninite, or through kasolite ($PbSiUO_6\cdot 2H_2O$), a uranyl lead silicate.

In this study, samples from the unweathered, primary ore zone were analyzed to clarify the alteration processes which caused the alteration of uraninite to uranyl silicates. These data are used to model the geochemical redistribution of uraium from uraninite (UO_{2+x}) in contact with flowing ground water.

Samples and Experimental Techniques

Four specimens were taken from the drill core samples at the Koongarra research site. They were selected by observations of uranium minerals by naked eye to repesent the unweathered, primary ore zone of pitchblende

with U-Pb oxides and the uranyl silicate zone. Three samples are from a core hole (DDH58) at vertical depths from the surface of 30.1 m (DDH58-129), 30.6 m (DDH58-131) and 31.0 m (DDH58-132), respectively. Another specimen (DDH9-151) was from DDH9 core sample (35.3 m). Petrologic thin sections were made from these rocks for observations by optical microscopy (OM) and backscattered electron imaging (BEI). Quantitative chemical analyses were performed on a JEOL 733 Superprobe electron microprobe analyzer (EMPA) with a focused beam of 1 μm in diameter and beam current of 20 nA.

Results and Discussion

By the OM, BEI and EMPA observations, the most abundant uranium mineral was sklodowskite, a uranyl-Mg silicate ($MgSi_2U_2O_{11}\cdot 7H_2O$). Primary uraninite was observed in a sample and it was surrounded by curite and wölsendorfite ($PbU_2O_7\cdot 2H_2O$), uranyl-Pb oxide, and sklodowskite. Kasolite is observed within Pb-free sklodowskite veins in the uranyl silicates region. Kasolite crystals are euhedral and acicular. These observations suggest that alteration of primary uraninite did form only sklodowskite and U-Pb oxide minerals and kasolte precipitated from sklodowskite. Detailed description and compositions of the samples were appeared in Isobe et al.[6].

The composition of the minerals obtained from sample DDH58-129 shows that the conversion of primary uraninite to sklodowskite and curite is as follows:

$$\underset{\text{primary uraninite}}{U_{17.6}Pb_{2.7}Ca_{2.0}X_{1.3}O_{46.7}} + 8.0Si^{4+} + \underset{\text{ground water}}{3.6Mg^{2+}} \rightarrow$$

$$\underset{\text{curite}}{U_{8.0}Pb_{2.7}X_{0.4}O_{27.0}\cdot 5H_2O} + \underset{\text{sklodowskite}}{Mg_{3.6}Ca_{0.6}Si_{8.0}U_{9.6}X_{0.9}O_{52.8}\cdot 33.6H_2O} + 1.4Ca^{2+}, \quad (1)$$

where X represents minor components such as K or P. Mass balance and valence of O, H_2O and X are not considered. According to this reaction, and accounting for the densities of the phases, primary uraninite (100 relative volume units) altered to curite (69 units) and sklodowskite (173 units). The expanded sklodowskite "filled-in" the morphology of the pri-

mary uraninite, and the excess sklodowskite was observed in many veinlets surrounding the uraninite. These calculations depend on the current Pb-content of the uraninite. Because radiogenic Pb was produced continuously in uraninite, the Pb-content of the uraninite undergoing alteration must be less than to the current value. Thus, the relative volume of curite as alteration product must be less than 69 units when the altered minerals were first formed. The modal ratio of curite is less than 50%, and this may reflect a lower Pb-content for uraninite at the time of alteration. Consequently, the modal volume ratio of curite, smaller than that expected from the current Pb-content in uraninite, does not support Pb-release from uraninite. Therefore Pb was not released from uraninite to form kasolite when Si and Mg were in ground water.

Pb was enriched in the residual U-Pb oxide within the primary uraninite grains to a greater degree than if the radiogenic Pb-content of pure uraninite was the same age as the Koongarra mineralization. In some grains, Pb-enrichment in residual grains brings the Pb-content of the grain up to 25 wt.%, which is more than that of curite. Wölsendorfite was observed in the grains with a high Pb enrichment.

The formation of Kasolite from the radiogenic Pb in sklodowskite causes volume decrease. This results in the formation of veins within the sklodowskite, and these veins are pathways for ground water movement. Consequently, the formation of kasolite from sklodowskite promotes the mobility of the ground waters and elements therein. On the other hand, the volume of alteration products of uraninite or U-Pb oxides is more than twice that of the original uraninite. In this case, volume expansion may hinder ground water movement. Thus, the alteration mechanisms of uraninite and the U-Pb oxides may be essentially different from that of uranyl silicate minerals in Koongarra.

Another component in the primary uraninite, Ca, is released from the uraninite during the alteration process as described in the equation (1). In this study, uranophane ($CaSi_2U_2O_{11}\cdot 6H_2O$) was not identified in any specimens. The Ca-content was significantly low (less than 0.2 wt.% as CaO) in the U-Pb oxides and uranyl silicates. Calcium concentrations of the major phases of the host rock, such as chlorite and mica were also low. Apatite was observed as an accessory mineral in all the samples, but it may be an insufficient source of Ca. The Ca-concentration in the ground water in Koongarra was 2 mg/L, and this was one tenth of the Mg concentration in the ore region. Calcium released from the uraninite may

be mobile in ground water due to its low concentration. The Pb-content in the ground water was also low (0.5~1 μg/L), and the atomic ratio of Pb/Ca was less than 1×10^{-4}(7). This may be not enough to transport Pb from the primary ore region and to form minerals containing Pb.

Conclusion

The alteration processes in the unweathered zone of the Koongarra ore body are characterized as follows: 1) Low Pb-mobility and high Ca-mobility from the primary uraninite. This resulted Pb-rich residual phases such as curite and wölsendorfite within the altered uraninite but kasolite was not formed within the altered uraninite. 2) Precipitation of kasolite from radiogenic Pb released from sklodowskite, and these minerals kept their stoichiometric compositions (Fig. 1). The preferred alteration reactions are affected by the volume changes between reactants and products, the composition of the whole host rock and the ground water chemistry.

References

1. Ewing, R.C.: Natural systems prediction of radionuclide migration. in Proc. on The 3rd International Symposium on Advanced Nuclear Energy Research -Global Environment and Nuclear Energy- Japan Atomic Energy Research Institute, Mito, (1991).
2. Airey, P.L. and Ivanovich, M.: Geochemical analogues of high-level radioactive waste repositories. Chemical Geology 55 203-213 (1986).
3. Duerden, P.: Alligator Rivers Analogue Project, 1st Annual Report 1988-1989, Australian Nuclear Science and Technology Organisation, Australia, (1990).
4. Franco, P. Trocellier, P. and Menes, F.: UO_2 corrosion study in mineral water: a surface analysis approach. in Scientific Basis for Nuclear Waste Management XII, eds. C.M. Jantzen, J.A. Stone and R.C. Ewing, Materials Research Society, 343-349 (1989).
5. Snelling, A.A.: Uraninite and its alteration products, Koongarra uranium deposit. in Uranium in the Pine Creek Geosyncline, eds. J. Ferguson and A.B. Goleby, International Atomic Energy Agency, Vienna, 478-498 (1980).

6. Isobe, H., Murakami, T. and Ewing, R.C.: Alteration of uranium minerals in the Koongarra deposit, Australia: Unweathered zone. Journal of Nuclear Materials 190 174-187 (1992).
7. Duerden, P.: Alligator Rivers Analogue Project, Progress Report 1 March 1990 - 31 May 1990, Australian Nuclear Science and Technology Organisation, Australia, (1990).

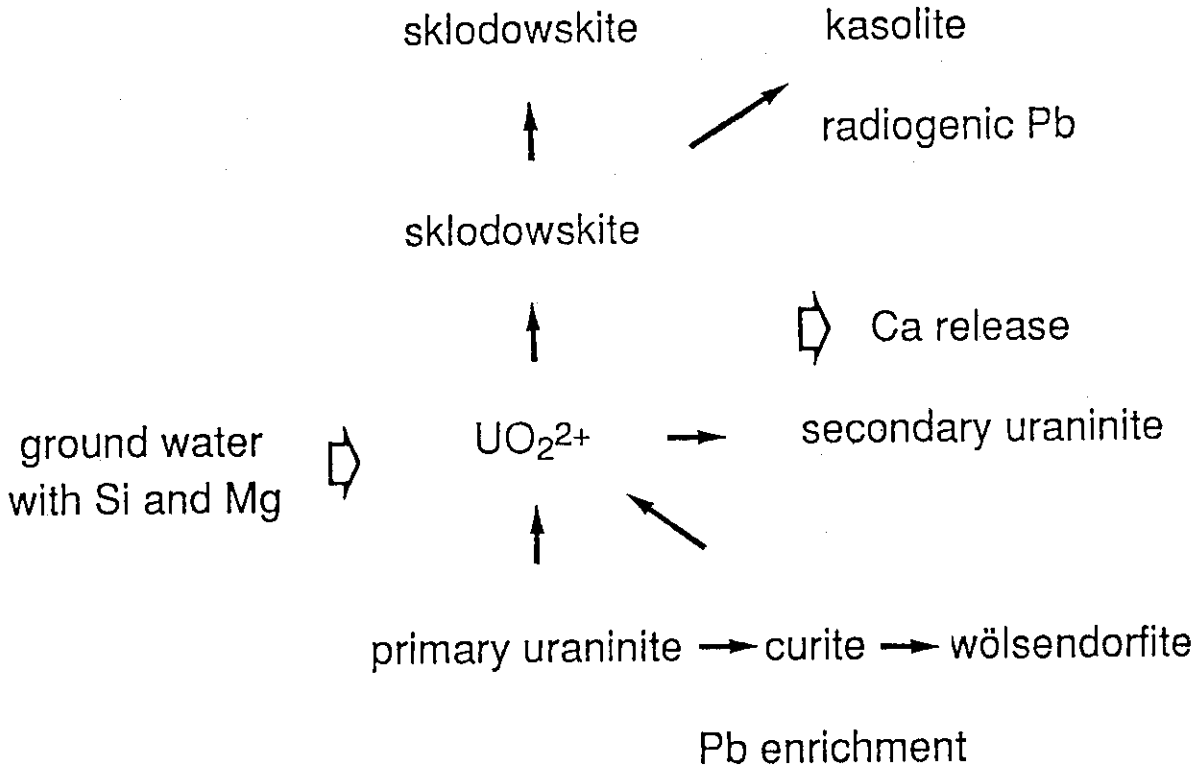

Fig. 1 Schematic diagram of the alteration paths from primary uraninite to uranyl silicates. Uraninite and U-Pb oxide supply only uranium to form uranyl silicates. Lead in kasolite derives from radiogenic Pb in the sklodowskite.

3.3 Uranium Fixation during Chlorite Weathering at Koongarra, Australia

T. Murakami, H. Isobe, T. Ohnuki, T. Nagano and S. Nakashima

Introduction

Quartz-chlorite schist, the host rock in the vicinity of the ore deposit at Koongarra, Australia, has probably been subjected to weathering for more than one million years. Although quartz is resistant to the weathering, chlorite has been altered to clay minerals (vermiculite to kaolinite) and iron minerals. Similarly, part of the uranium, mineralized as uraninite originally, has been weathered to be uranyl silicates such as sklodowskite, kasolite, uranophane. Part of the uranyl silicates has been further weathered to form uranyl phosphates such as saléeite in "the economic secondary ore deposit"[1]. Of major interest to the disposal of high level radioactive waste is "the dispersion fan", downstream of the ore deposits, where uranium is associated with the alteration products of chlorite. Such an association can be a good analogue of the fixation of radionuclides to rocks and also can simulate nuclide migration through rocks.

We have noted that the uranium redistribution is affected by the chlorite weathering, and shown that the uranium concentrations in minerals increase with increase in the extent of the weathering[2]. The uranium at Koongarra is closely related to the iron minerals, but the uranium-iron association has not been analyzed non-destructively before. In this paper, we will describe the uranium-iron association with emphasis on the chemical forms of iron-uranium associated materials by visible microspectroscopy.

Sample Description

Koongarra samples. Fifteen diamond-drilled cores, 70-120 m long, were visually inspected at Koongarra. Sample DDH4-99 used in the spectroscopic and elemental-analytical measurements below, was located 23 m deep from the surface, in the so-called transition zone. Spatially, the sample was about 60 m downstream of the end of the economic zone of secondary ore[1].

Uranium minerals. Specimens of kasolite, $Pb(UO_2)SiO_4H_2O$, sklodowskite, $Mg(H_3O)_2(UO_2)_2(SiO_4)_2.4H_2O$, and saléeite, $Mg(UO_2)_2(PO_4)_2.10H_2O$, were also collected at Koongarra and used as references in the spectroscopic and elemental-analytical measurements. These minerals are often seen in the ore deposits as is uraninite, UO_2, the primary uranium mineral. The alteration sequence of uraninite-kasolite-sklodowskite-saléeite has been reported[1]. In general, the uranium oxides and silicates are present in the primary ore deposit and the uranium phosphates are found in the secondary ore deposit[1]. The kasolite and sklodowskite specimens used here are from sample DDH58-130 and the saléeite is from DDH65-95. These uranium minerals were identified by color, fluorescence at room and liquid nitrogen temperature, electron microprobe data, and the occurrence of uranium minerals at Koongarra[1].

Experimental Techniques

The mineralogical textures of the samples were examined by optical microscopy (OM) and scanning electron microscopy (SEM). Elemental analyses were made qualitatively by electron microprobe analysis (EMPA), using petrologic thin sections for DDH4-99, kasolite and sklodowskite, and powders for saléeite. The chemical forms of uranium and iron of the specimens were examined by transmission visible microspectroscopy (VIS) (microscopic spectrophotometer Hitachi U-6500), using the thin sections. The analyzed area was 3 or 5 μm in diameter.

Visible Spectra of Iron and Uranium Minerals

Uranium is found to be distributed along fractures at Koongarra and the weathering products along the fractures are primarily responsible for the uranium association[2]. The sequential extraction and sorption data show that iron minerals, are possibly more associated with uranium than other weathering products such as kaolinite, vermiculite[3,4,5]. The iron minerals occurring at Koongarra are goethite, hematite[6], and ferrihydrite (or amorphous iron hydroxide)[4]. We initially examined the iron minerals and possible uranium minerals by visible spectroscopy.

Figure 1 shows the spectra of goethite, hematite, and $Fe(OH)_3$ (amor-

phous iron hydroxide) by diffuse reflectance spectroscopy[7,8]. Hematite has a plateau from 390 to 550 nm and a steep slope from 550 to 600 nm while $Fe(OH)_3$ has a rather gentle slope down to around 650 nm, a very broad, weak band at around 500 nm. Goethite is characterized by a point of inflection at 480 nm. We did not analyze the iron-mineral contents of the specimens quantitatively but did qualitatively by the three different spectroscopic patterns.

Possible uranium compounds associated with the iron minerals are uranium minerals existing at the ore deposits, such as uranium oxides, uranyl silicates and uranyl phosphates[1], and aqueous uranyl species such as uranyl hydroxy complexes and uranyl carbonate complexes[5]. Kasolite and sklodowskite (uranyl silicates) and saléeite (uranyl phosphate) were chosen for the spectroscopic measurements because of their extensive occurrence at the Koongarra deposits[1]. Uraninite (UO_2) was excluded because uranium in the transition and weathered zones is oxidized to be in higher valence states (uranyl species) but not in the form of U^{4+}. As a reference for aqueous uranyl species, 0.00915 mole $UO_2(ClO_4)_2$ in 0.0014 mole $HClO_4$[9] was used and this is hereafter referred to as free-uranyl.

The microscopic visible spectra of the uranyl minerals and species are given in Fig. 2. The uranyl silicates have absorbance bands in the region of 400-470 nm; kasolite has a broad band at around 430 nm while sklodowskite has fine structures (peaks at 400, 410, 421, 430, 442, 456, and 470 nm) and an absorption maximum at 420 nm (Fig. 2). The main bands (420-440 nm) of the two uranyl silicates are shifted to each other by around 10 nm. On the other hand, saléeite has distinct peaks at 401, 412, 424, and 436 nm in the region of 400-450 nm (Fig. 2). The spectroscopic pattern and peak positions of saléeite are almost the same as those of autunite, another uranyl phosphate, $Ca(UO_2)_2(PO_4)_2.10H_2O$[10]. Although the spectroscopic pattern of sklodowskite appears different from that of saléeite, the peak positions of the two minerals are similar to each other. The spectrum of the free-uranyl has the same pattern as that of saléeite but the absorption maximum of the free-uranyl is shifted by about 10 nm with respect to that of saléeite.

Visible Spectra of Koongarra Specimen

Uranium was detected in the Fe-rich veins by EMPA but not found away

from the vein. However, this does not mean that uranium does not exist out of the Fe-rich veins. Indeed, uranium is often found by alpha autoradiography[2] in vermiculite and the other weathered products.

Figure 3 shows transmission visible spectra at the analytical points A (DDH4-99-A) and B (DDH4-99-B). The spectroscopic patterns are different from those of unweathered chlorite and partially weathered chlorite (vermiculite and iron minerals)(Fig. 4). The latter spectra are much less influenced by the iron minerals. Fully weathered chlorite has a similar spectroscopic pattern to that of goethite (bands at 480 nm in Fig. 1). Thus, as the weathering of chlorite proceeds, iron minerals, especially goethite, are accumulated in mineral grains. The results of the spectroscopic measurements are in good agreement with those of the SEM observations[2]; viz, during the weathering, iron is released from chlorite and later from vermiculite, and accumulated.

By comparing the spectrum of DDH4-99-B to those of hematite, goethite, and $Fe(OH)_3$ (Fig. 1), the major iron mineral species at point B is found to be goethite. This result is supported by the transmission visible spectrum of goethite in an andesite thin section under the same measurement conditions as those for DDH4-99-B[10]. The backscattering image and elemental analysis (Fig. 5a) show that iron is more concentrated in the iron veins, where point A is located, than in any other areas. The transmission visible spectrum of DDH4-99-A does not fit well to any individual spectrum or combination of the two spectra shown in Fig. 1. However, because the examination by OM and SEM indicates that iron minerals are present at point A, and because only hematite, goethite and ferrihydrite are the iron minerals detected at Koongarra, it was concluded that a mixture of the three iron minerals exists at point A.

Fine structures of DDH4-99-A and -B in the region of 400 to 450 nm (Fig. 3) are compared to those of uranyl species (Fig. 2). The fine structures are different in pattern and peak positions from those of kasolite and sklodowskite, but are similar to those of saléeite and the free-uranyl (Fig. 2). Because the fine structures of saléeite and the free-uranyl are similar to each other, it is difficult by only comparing the visible spectra to determine which uranyl species is present with the iron minerals. Hence we used EMPA to determine which elements coexist at the analytical points. At point A, uranium was found, and importantly, phosphorous was also detected though at point B neither uranium nor phosphorous was detected (Fig. 5). Magnesium was also present at point A.

It should be noted that EMPA is less sensible than VIS. The EMPA spectra suggest that either the uranyl silicates or free uranyl is not the uranyl species coexisting with the iron minerals, and that the most possible uranyl species is magnesium uranyl phosphate, that is, saléeite. The presence of saléeite at point A is not inconsistent with the EMPA pattern of saléeite (Fig. 5). Saléeite is the most common uranyl phosphate in the secondary ore deposit[1], and the other uranyl phosphates such as renardite, $Pb(UO_2)_4(PO_4)_2(OH)_4.7H_2O$, are not consistent with the EMPA spectrum of DDH4-99-A. Although the most possible uranyl species coexisting with the iron minerals is saléeite, we cannot exclude the possible existence of the free-uranyl because of its similar absorption maximum at around 414 nm to that of DDH4-99-B.

Discussion

Our results suggest that the U-Fe relationship mostly occurs as a mixture of hematite, goethite, and ferrihydrite, and saléeite in Fe-rich veins, and possibly at grain boundaries and along fractures. Some uranium is fixed to goethite-predominant iron minerals in weathered chlorite grains. Uranyl ion complexes such as uranyl phosphate ions may be present in groundwater at Koongarra[11]. Such uranyl ion complexes can be sorbed as free uranyl by ferrihydrite. The absorption maximum at around 412 nm of DDH4-99-B may result from free uranyl of the uranyl ion complexes. However, it is unlikely that the uranyl ion complexes have been attached to the iron minerals for a million years without any change in their forms. Thus, the uranium and phosphorus peaks appearing in the EMPA spectrum cannot be interpreted as those of uranyl phosphate ions. Even if uranyl ion complexes are sorbed by ferrihydrite and fixed to the iron minerals, the complexes may be crystallized to form saléeite.

The present study suggests that possible main uranium fixation and redistribution mechanisms are as follows:
Ferrihydrite, a direct byproduct of chlorite weathering[2], either co-precipitates with saléeite microcrystals, or complexes with a uranyl phosphate ion which is then crystallized to form saléeite. Goethite and hematite quickly dominate ferrihydrite because the half conversion of ferrihydrite to geothite and hematite takes only about a hundred days[12]. The ferrihydrite conversion is much faster than the chlorite to vermicu-

lite conversion[13]. The iron minerals move to be accumulated in grain boundaries, microfissures, and fractures[2] with retaining uranium.

Although the groundwater at Koongarra is currently undersaturated with respect to saléeite, the presence of saléeite in the secondary ore deposit suggests that the groundwater has previously been saturated. It is, therefore, more probable that saléeite at the sampling point of DDH4-99, 60 m away from the end of the secondary ore deposit, was formed synchronously (in the geological time scale) with the saléeite in the secondary ore deposit. The differences between the saléeites are in their concentrations and associated materials; if the concentration is high, saléeite precipitates by itself (i.e., in the secondary ore deposit), and if it is not high enough, saléeite coprecipitates with the iron minerals (i.e., at the sampling point of DDH4-99). Currently, saléeite may be dissolving and uranium is migrating further downstream.

Because ferrihydrite is very quickly converted to hematite and/or goethite, ferrihydrite would not exist for a geologically long time. However, ferrihydrite possibly exists at Koongarra. In order to understand the uranium redistribution thoroughly, it is necessary to confirm the presence of ferrihydrite in the iron-rich veins as well as the origin of ferrihydrite existing at the present time.

References

1. A.A. Snelling, Uraninite and its alteration products, Koongarra uranium deposit, in Proceedings of IAEA International Symposium Uranium in the Pine Creek Geosyncline, edited by J. Ferguson and A.B. Goleby (IAEA, Vienna 1980) pp. 487-498.
2. T. Murakami, H. Isobe and R. Edis, Effects of chlorite alteration on uranium redistribution in Koongarra, Australia, Scientific Basis for Nuclear Waste Management XIV, 741-748 (1991).
3. R. Edis, The redistribution of uranium series radionuclides at Koongarra, Scientific Basis for Nuclear Waste Management XIV, 727-732 (1991).
4. N. Yanase, T. Nightingale, T. Payne and P. Duerden, Uranium distribution in mineral phase of rock by sequential extraction procedure, Radionuchim. Acta 52/53, 387-393 (1991).
5. T.E. Payne and T.D. Waite, Surface complexation modelling of uranium

sorption data obtained by isotope exchange techniques, Radiochim. Acta 52/53, 487-493 (1991).

6. K. Sekine, T. Ohnuki, T. Murakami and H. Isobe, Migration behavior of uranium series nuclides in altered quartz-chlorite schist, in Alligator Rivers Analogue Projects, 1st Annual Report 1988-89, edited by P. Duerden, Australian Nuclear Science and Technology Organisation, Sydney, 103-111 (1990).
7. T. Nagano and S. Nakashima, Study of colors and degrees of weathering of granitic rocks by visible diffuse reflectance spectroscopy, Geochim. J. 23, 75-83 (1989).
8. T. Nagano, unpublished work.
9. J.T. Bell and R.E. Biggers, J. Mol. Spectrosc. 18, 247-275 (1965), in Gmelin Handbook of Inorganic Chemistry 8th Ed., Uranium, Supplement vol. A5, Springer-Verlag, Berlin (1982).
10. S. Nakashima, unpublished work.
11. T.E. Payne, J.A. Davis and T.D. Waite, Modelling of uranium sorption to substrates from the weathered zone in the vicinity of the Koongarra ore body, in Alligator Rivers Analogue Project 1st Annual Report 1988-89, P. Duerden (Ed.), Australian Nuclear Science and Technology Organisation, Sydney, 39-46 (1990).
12. U. Schwertmann and E. Murad, Effects of pH on the formation of goethite and hematite from ferrihydrite, Clays and Clay Minerals 3, 277-284 (1983).
13. T. Murakami, T. Ohnuki and T. Sato, Kinetic analysis of chlorite alteration, Abstr. Fall Meeting of the Mineral. Soc. Japan (with English abstracts), Sendai (1991).

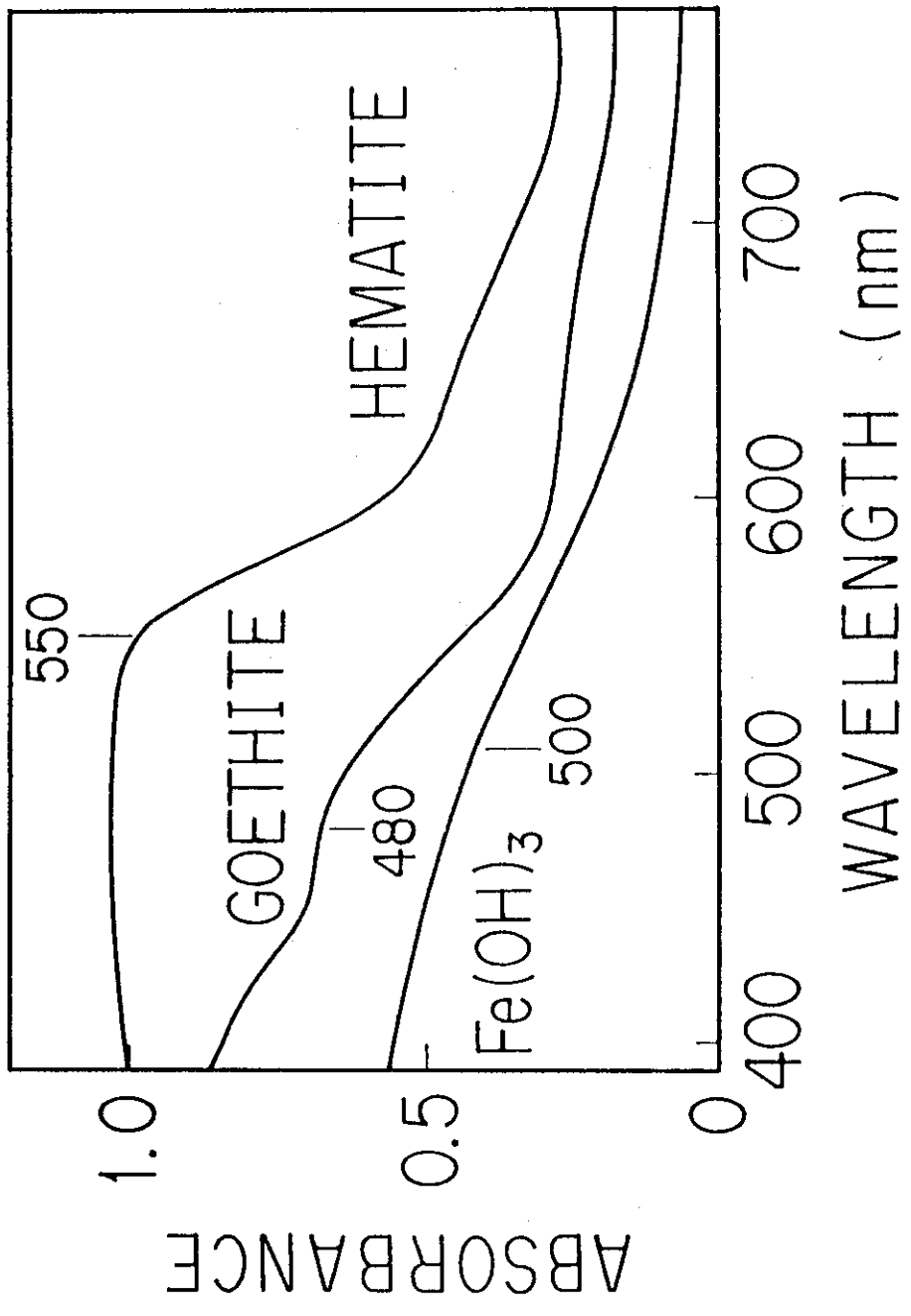

Fig. 1 Visible diffuse reflectance spectra of hematite and goethite (from Nagano and Nakashima[7]) and amorphous iron hydroxide, $Fe(OH)_3$ (from Nagano[8]).

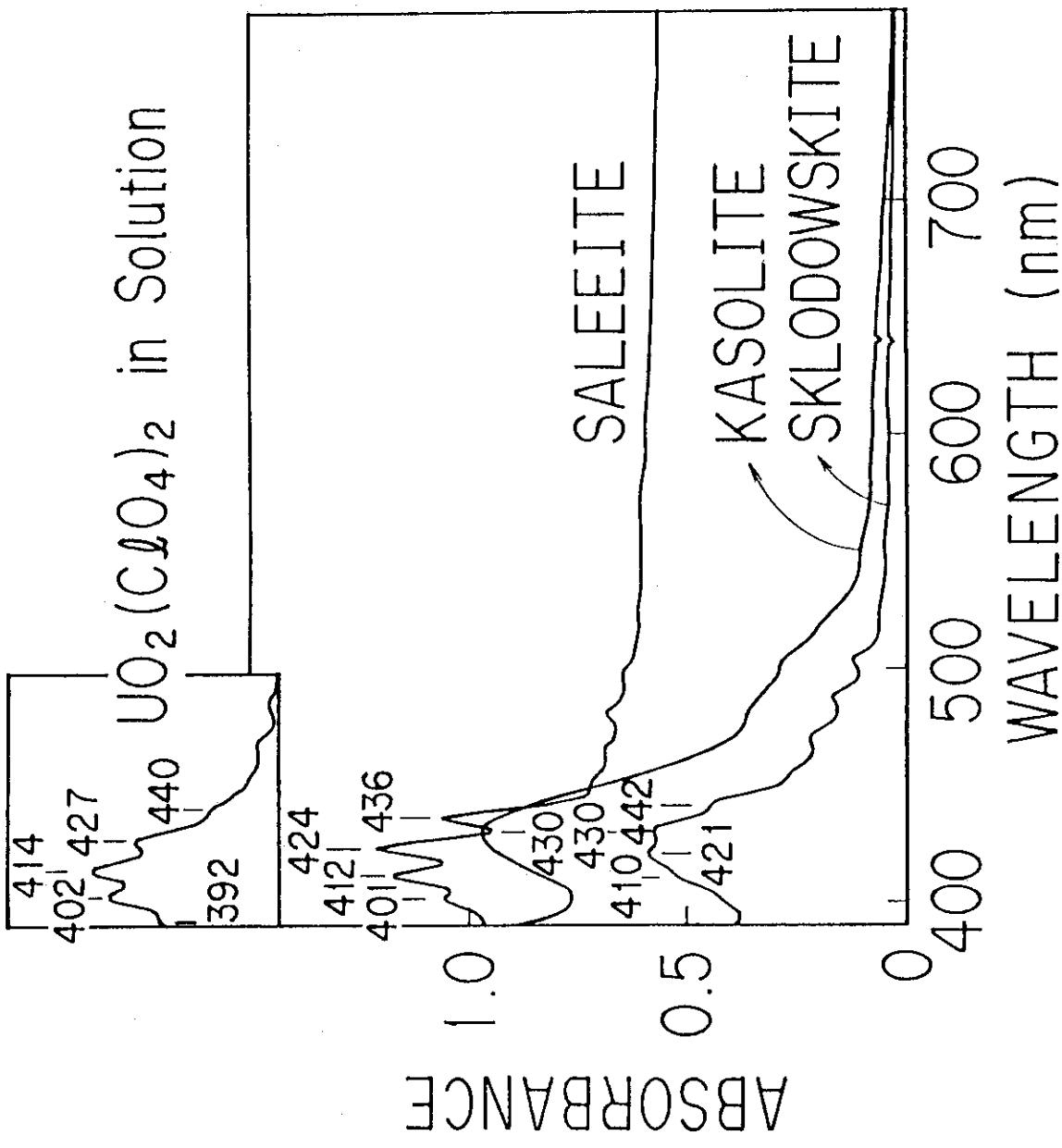

Fig. 2 Transmission visible spectra of kasolite, sklodowskite, and saléeite with a visible spectrum of $UO_2(ClO_4)_2$ (from Bell and Biggers[9]) in the inlet.

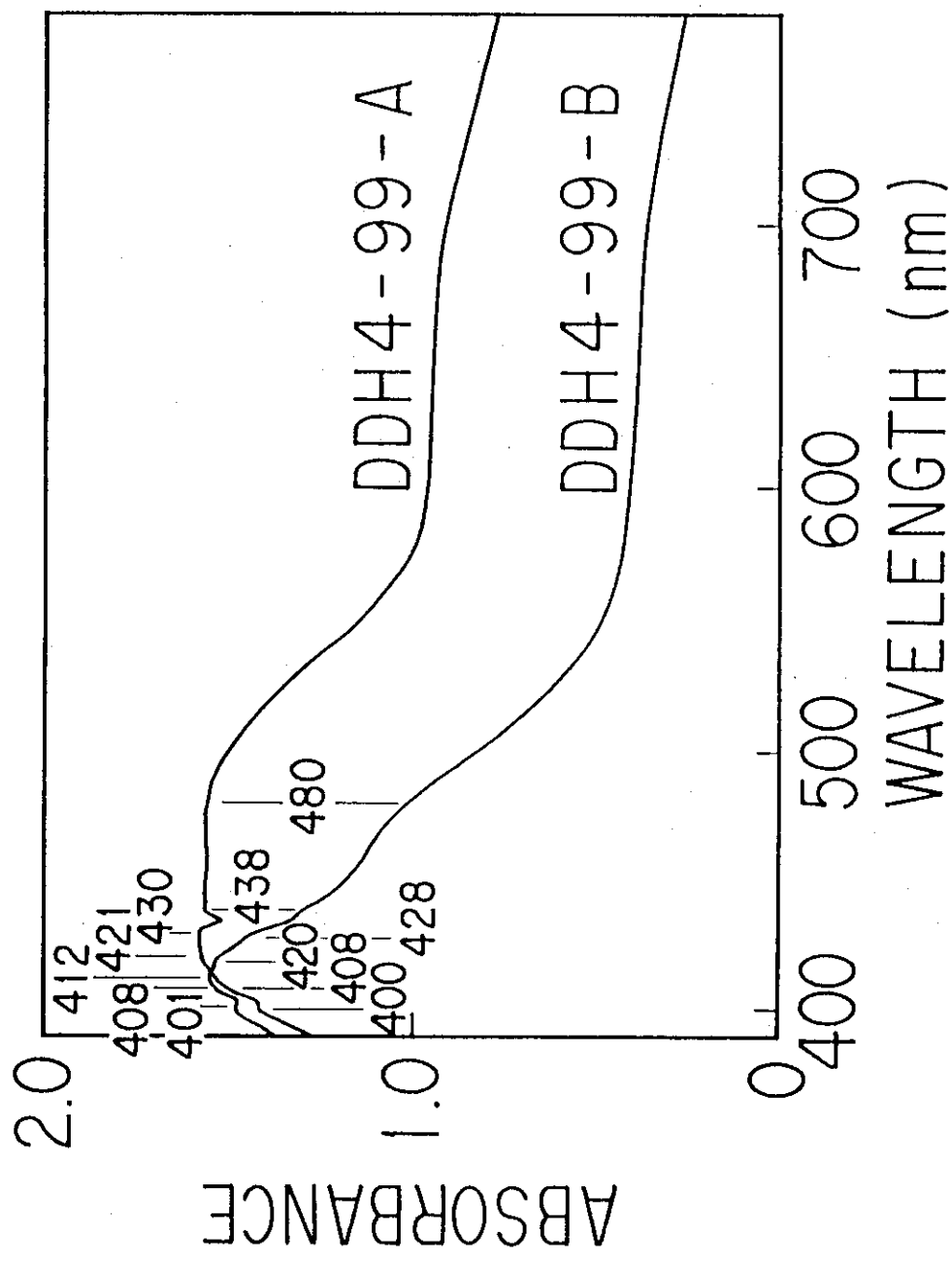

Fig. 3 Transmission visible spectra of DDH4-99-A and -B.

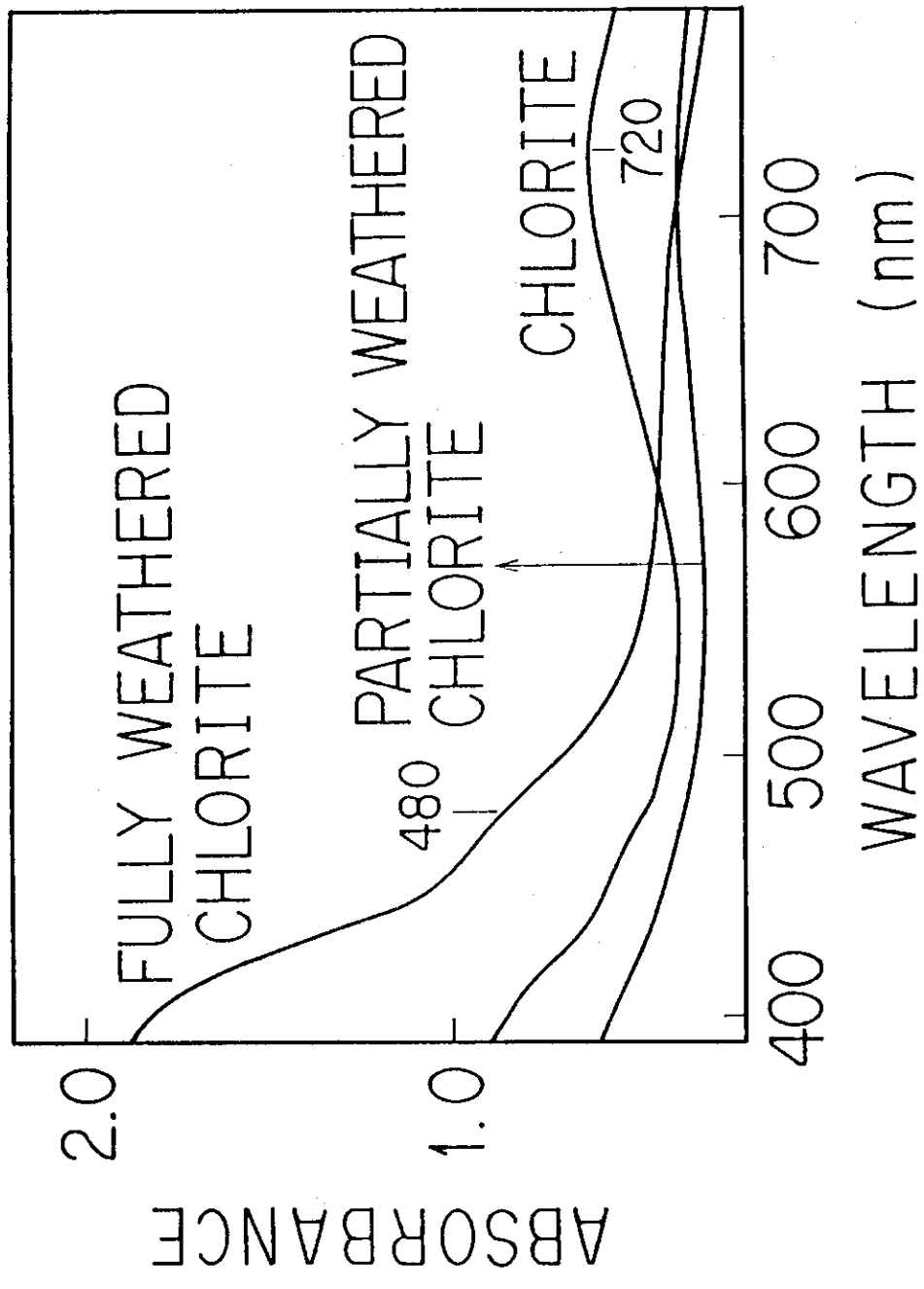

Fig. 4 Transmission visible spectra of unweathered chlorite, partially weathered chlorite (vermiculite and iron minerals), and fully weathered chlorite (kaolinite and iron minerals). The spectra of unweathered chlorite and partially weathered chlorite are very different from those of DDH4-99-A and -B in Fig. 3.

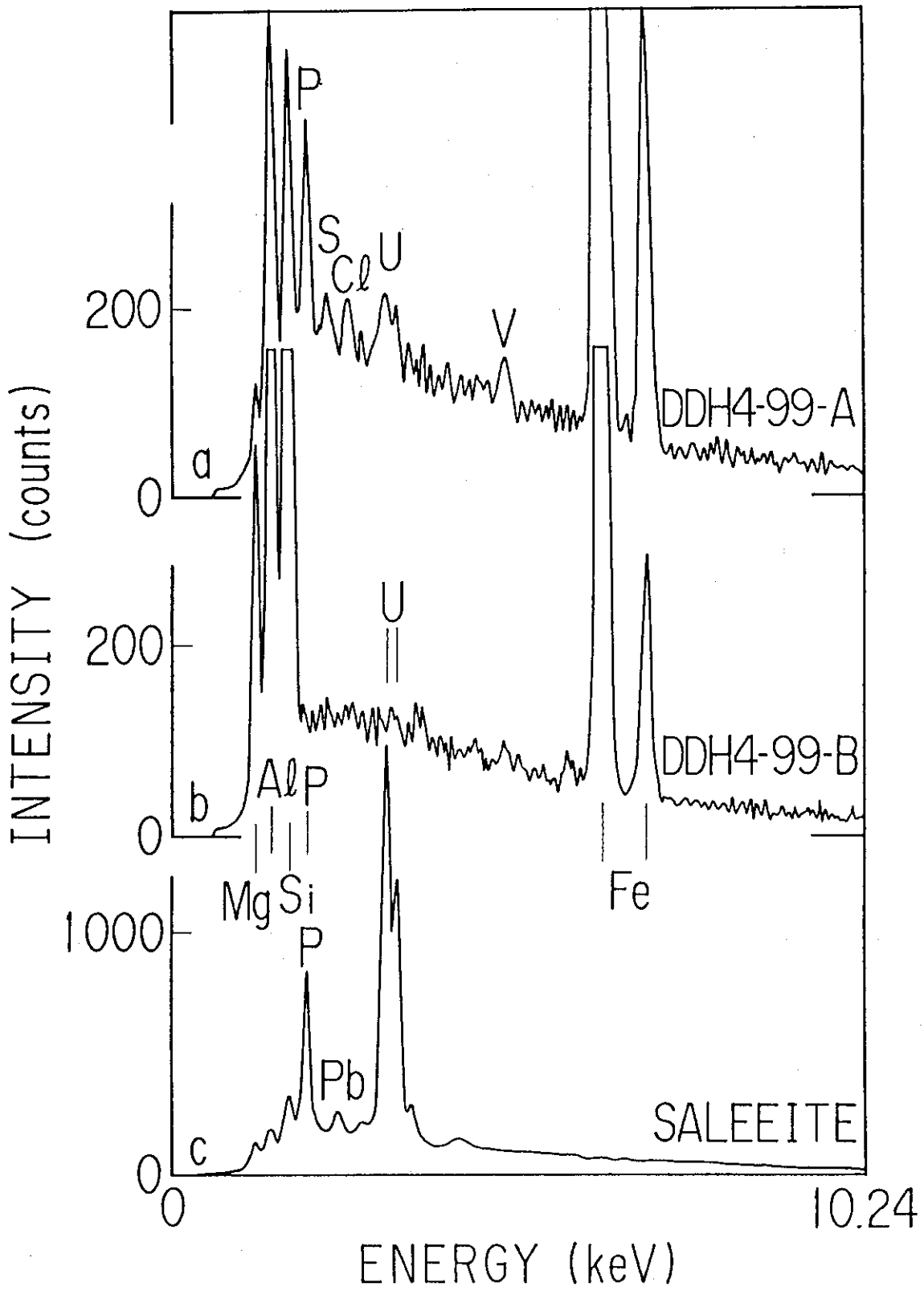

Fig. 5 Spectra of DDH4-99-A (a) and -B (b), and saléeite (c) by electron microprobe analysis. Uranium is present along with phosphorus in DDH4-99-A but either uranium or phosphorus is not detected in DDH4-99-B.